

## The Sensitivity of Simulated Supercell Structure and Intensity to Variations in the Shapes of Environmental Buoyancy and Shear Profiles

EUGENE W. McCAUL JR.

*Universities Space Research Association, Huntsville, Alabama*

MORRIS L. WEISMAN

*National Center for Atmospheric Research,\* Boulder, Colorado*

(Manuscript received 10 December 1999, in final form 5 September 2000)

### ABSTRACT

Convective storm simulations are conducted using varying thermal and wind profile shapes, subject to the constraints of strict conservation of convective available potential energy (CAPE) and hodograph trace. Small and large CAPE regimes and straight and curved hodographs are studied, each with a matrix of systematically varying thermal and wind profile shapes having identical levels of free convection and bulk Richardson numbers favorable to supercell development. Differences in storm intensity and morphology resulting from changes in the profile shapes can be profound, especially in the small CAPE regime, where, for the moderate shears studied here, storms are generally weak except when the buoyancy is concentrated at low levels. In stronger CAPE regimes, less dramatic relative enhancements of storm updraft intensity are found when both the buoyancy and shear are concentrated at low levels.

Peak midlevel vertical vorticity correlates roughly with peak updraft speed in the small CAPE regime, but it shows less sensitivity to buoyancy and shear stratification at larger CAPE. Although peak low-level vertical vorticity can be large in either CAPE regime, it is generally larger in the large CAPE regime, where evaporation of rain leads to the formation of stronger surface cold pools, zones of enhanced horizontal shear, and baroclinic production of horizontal vorticity that can be tilted onto the vertical by storm updrafts. The present parameter space study strongly suggests that, while bulk CAPE and shear are important determinants of gross storm morphology and intensity, significant modulation is possible within a given bulk CAPE and shear class by changing only the shapes of the profiles of buoyancy and shear, either alone or in combination.

### 1. Introduction

Prior studies have shown the importance of bulk or integral environmental quantities such as convective available potential energy (CAPE) and 0–6-km mean vertical shear for convective storm structure and intensity (Weisman and Klemp 1982, 1984). These studies found that, for buoyancy and wind profiles approximating those commonly found in midlatitude severe storm environments, a bulk Richardson number given by the ratio of the total CAPE to the kinetic energy in the storm-relative inflow (the latter expressed as half the square of a vector related to the 0–6-km shear)

served as a good predictor of whether a storm would display multicell or supercell characteristics. This distinction is important because supercell storms tend to be unusually severe and persistent, and they account for a disproportionately large share of tornadoes and other severe weather manifestations at the surface. In the Weisman and Klemp studies, the starting environments for cloud-scale simulations were specified using analytical functions that yielded a range of CAPE and vertical shear values, but the resulting buoyancy profiles featured maxima at different altitudes, the simulated storms had different levels of free convection, and there was no linkage between the functions describing the shapes of the buoyancy and shear profiles. These limitations also apply to other parameter space studies based on the Weisman and Klemp profiles (see, e.g., Richardson et al. 1998).

Many other investigators have studied the impact on simulated convection of variations in the low-level or midlevel vertical shear. Droegemeier et al. (1993) considered the effects of hodograph turning using wind profiles all having the same shears. Brooks et al. (1994)

\* The National Center for Atmospheric Research is sponsored by the National Science Foundation.

*Corresponding author address:* Eugene W. McCaul Jr., Institute for Global Change Research and Education, 4950 Corporate Drive, Suite 200, Huntsville, AL 35806.  
E-mail: mccaule@space.hsv.usra.edu

simulated storms in environments having varying mid-level shears, but identical 0–3-km curved hodographs. Wicker (1996) studied the effects of variations of the low-level shear alone.

Recent studies of storms simulated in landfalling hurricane environments (McCaul and Weisman 1996) have shown that supercells can develop even when CAPE values are as small as  $600 \text{ J kg}^{-1}$ . In such cases, however, the supercells are smaller and shallower than those observed and simulated in larger CAPE environments. A salient feature of conditions commonly found in landfalling hurricanes is that parcel buoyancy is typically maximized near 3-km altitude, a position much lower in the troposphere than is usual for U.S. Great Plains severe storm environments, where buoyancy is often maximized in the 6–10-km altitude range. The hurricane environments also feature maximum winds in the lower troposphere, which presents a further contrast with the Great Plains environments. These aspects of the landfalling hurricane environment are described in some detail in McCaul (1991) and McCaul (1993).

Small supercells have also been observed in some midlatitude storm systems (Kennedy et al. 1993; Monteverdi and Quadros 1994; Knupp et al. 1998). In most such cases, proximity rawinsonde data suggest that CAPE is usually quite small, and that there is a tendency for the parcel buoyancy to reach a maximum at low altitudes in the cloud-bearing layer, much as in the landfalling hurricane environments.

The accumulation of evidence from many of these prior studies thus suggests that the shape of the buoyancy profile may have a strong effect on the characteristics of convective storms, especially supercells. Some of the data also suggest that there may be a synergistic interaction between the joint vertical stratifications of buoyancy and shear that can help promote the development of surprisingly intense convective storms in some small CAPE environments not traditionally thought conducive to severe convection. To study this basic storm physics question quantitatively for both small and large CAPE conditions, we have constructed, for each CAPE condition, a series of three initial buoyancy and wind profiles based on simple integral-conserving analytical expressions for the disposition of buoyancy and wind in the vertical, created all possible permutations of these starting profiles, and conducted cloud-scale numerical simulations using these environments.

The set of permutations of the profiles yields matrices of starting environments, each having constant CAPE and hodograph trace (here defined as the curve containing the hodograph, without regard for the altitude at which the various points on the hodograph occur), but with systematic variations in the altitudes of maximum buoyancy and of one component of wind. Both curved and straight hodograph traces are examined here. Separate matrices of starting environments are used for each value of bulk CAPE or hodograph trace radius

used. In addition to bulk CAPE and shear, all other environmental and numerical parameters that might significantly affect the simulated storms are also held constant within each matrix of simulations.

In section 2, we describe the characteristics of the buoyancy and wind profiles used in the simulations, and the initialization of the numerical model. The details of the analytical function formulation used in defining the profiles is relegated to the appendix. Section 3 contains text, tables, and graphs describing the results from the several matrices of simulations. Section 4 is devoted to a discussion of the findings, while section 5 presents a summary and prospectus for future research.

## 2. Methodology

For our simulation tests, we are specifically interested in using environments that are nominally within the supercell regime, such that the basic dynamics of the dominant cells in each simulation are all similar, and for which we feel the buoyancy–shear stratification effects should be most easily observed. For this purpose, we consider buoyancy and shear profiles that in combination are characterized by bulk Richardson numbers less than 45 (e.g., Weisman and Klemp 1982, 1984). Our approach, however, is quite general, and in future studies we will examine the stratification effects within other kinds of convective regimes.

Our environmental profiles are constructed using a constant-integral function that contains an amplitude parameter and a single shape compression parameter, referred to as  $m$  when applied to buoyancy, and  $n$  when applied to the wind, as described in the appendix. For both the buoyancy and wind profiles, the shape parameters  $m$  and  $n$  are both allowed to assume the values 2.2, 2.9, 4.0, and 7.0, which correspond to function maxima located at “scale” altitudes  $Z_b$  or  $Z_v$  of 7.1, 5.5, 4.1 and 2.5 km above ground level (AGL). These altitudes are approximately evenly spaced in the vertical, which facilitates interpretation of the simulation results. Note that larger values of the profile compression parameters correspond to larger low-level rates of change of the profile variable; lower-tropospheric lapse rates of temperature and vertical shear are thus controlled by the choice of profile compression parameter. In all discussion of our results, individual simulations will be identified using their  $Z_b$  and  $Z_v$  specifications.

We consider both a small CAPE regime ( $\text{CAPE} = 800 \text{ J kg}^{-1}$ ) and a larger CAPE regime ( $\text{CAPE} = 2000 \text{ J kg}^{-1}$ ). The 2000 CAPE regime represents environments similar to those seen in many midlatitude severe storm outbreaks, while the 800 CAPE regime resembles the environments seen in many landfalling tropical cyclones and other anomalous severe weather situations. The associated range of buoyancy profiles, expressed in terms of virtual potential temperature perturbations, are shown in Figs. 1a and 1b, while skew  $T$ – $\log p$  charts showing examples of the two extreme profile cases for

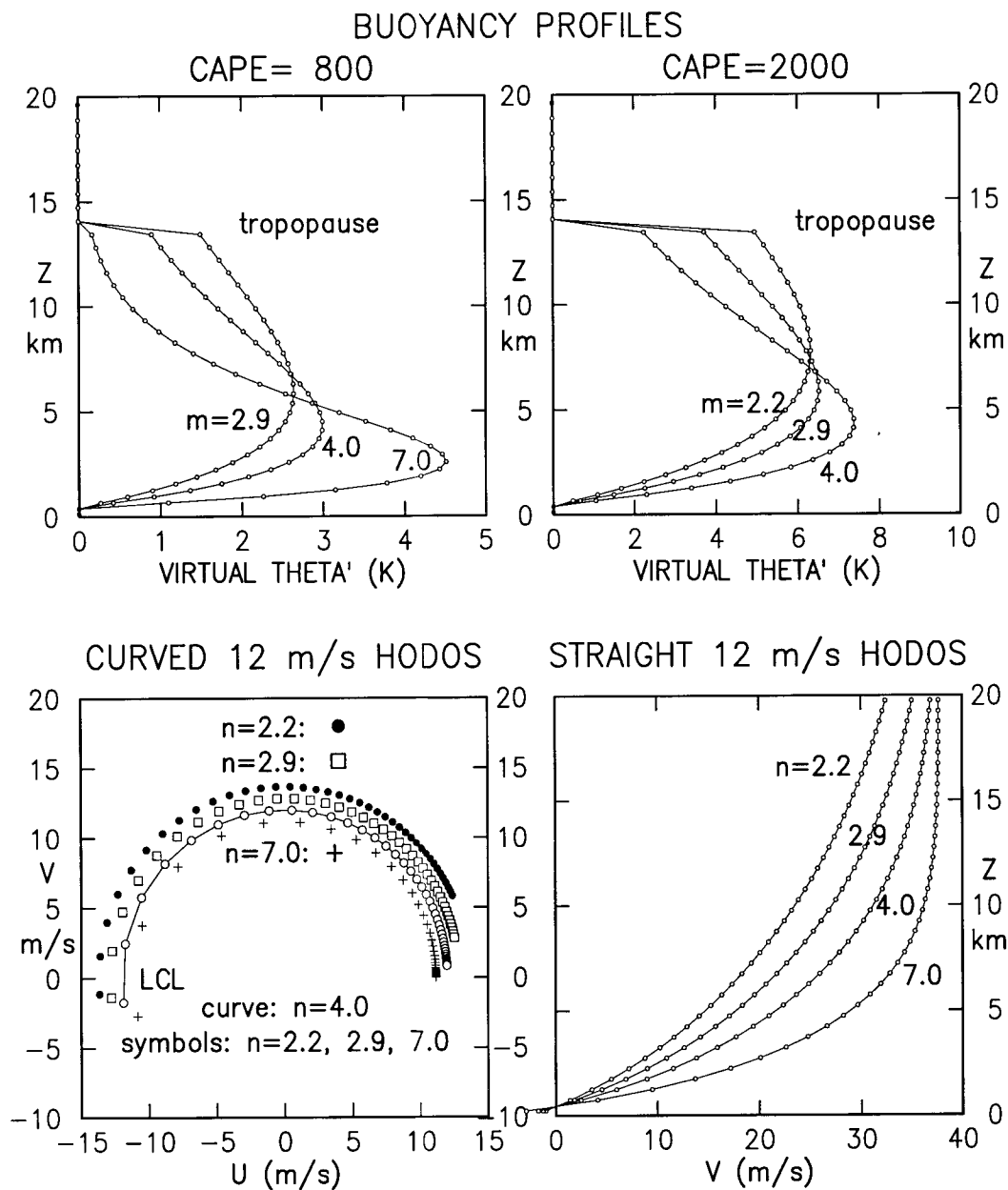


FIG. 1. Shapes of the various buoyancy and wind profiles used in the simulations, with buoyancy expressed in terms of perturbation virtual potential temperature (VIRTUAL THETA'). The buoyancy profiles are truncated by a tropopause at 14-km altitude. Untruncated versions of the profiles define the  $v$  wind component in the curved hodograph cases. Points on the hodographs are displayed for convenience using an unstretched vertical coordinate starting at  $z = 250$  m, with 500-m vertical discretization above. The straight hodograph profiles are obtained by unfolding the curved ones. Hodographs and  $v$  profiles associated with  $14 \text{ m s}^{-1}$  hodograph radii (not shown) resemble those shown, but with all values one-sixth larger.

both the  $\text{CAPE} = 800 \text{ J kg}^{-1}$  and  $\text{CAPE} = 2000 \text{ J kg}^{-1}$  regimes are presented in Figs. 2a and 2b, respectively. To enhance readability, the moisture and wind profiles are omitted from these charts.

Specification of the initial ambient wind profiles required more arbitrary decisions than did the construction of the buoyancy profiles. Prior theoretically based simulation work has focused primarily on idealized hodo-

graphs that are either straight (Weisman and Klemp 1982) or semicircular (Weisman and Klemp 1984). For maximum historical continuity between this work and previous studies, we have also chosen to study these same two kinds of profiles. As explained in the appendix, separate but related procedures were utilized in constructing the curved and straight hodograph wind profiles. For the curved hodograph cases, we applied our

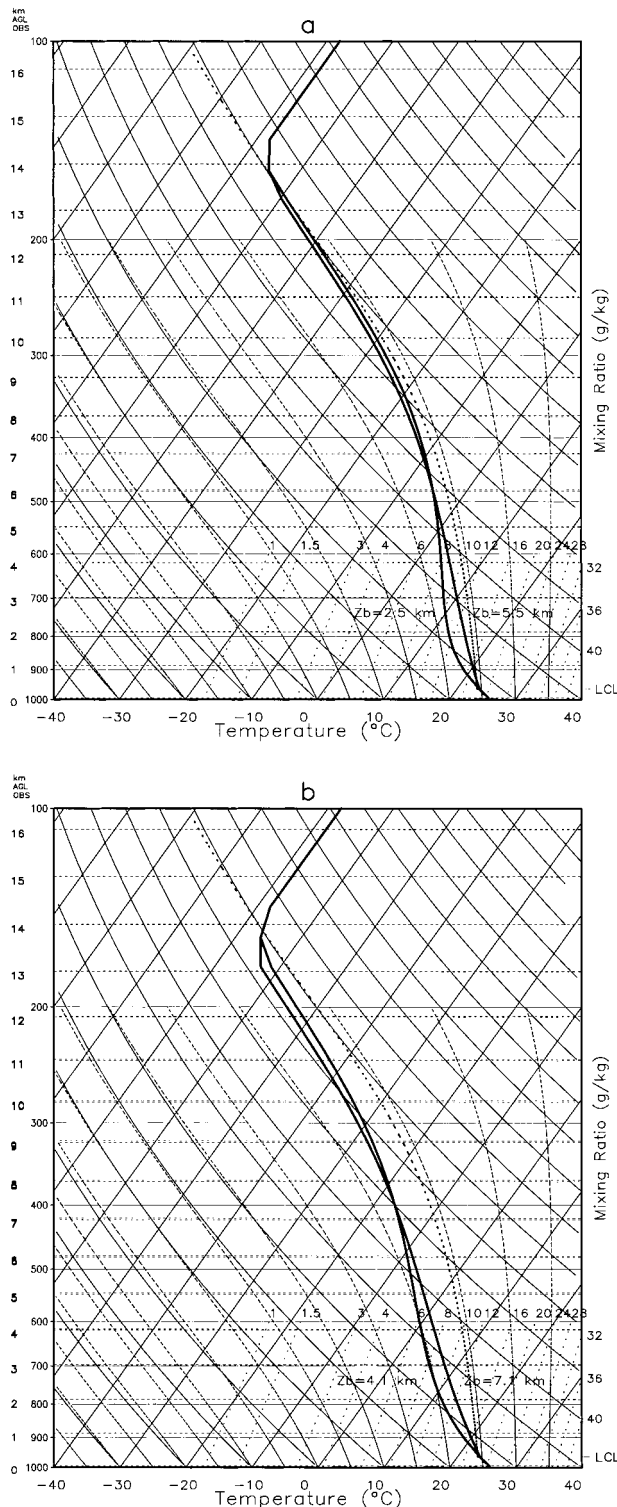


FIG. 2. Environmental temperature profiles for (a)  $\text{CAPE} = 800 \text{ J kg}^{-1}$  and hodograph radius  $V = 12 \text{ m s}^{-1}$  cases having  $Z_b = 2.5$  or  $5.5 \text{ km}$  and (b)  $\text{CAPE} = 2000 \text{ J kg}^{-1}$  and hodograph radius  $V = 12 \text{ m s}^{-1}$  cases having  $Z_b = 4.1$  or  $7.1 \text{ km}$ . Moisture profiles are omitted for clarity.

profile function to the  $v$  component of wind only in order to obtain our starting wind profiles, with the  $u$  component inferred from a constant hodograph radius constraint. For the straight hodograph cases,  $u$  was set to zero, and the  $v$  profiles were obtained by unfolding the curved hodographs, so that the vertical shear profiles were identical across curved and straight hodograph profiles having similar  $n$ .

The overall magnitude of the shear is defined by the parameter  $V$ , which is set to  $12 \text{ m s}^{-1}$  for the  $\text{CAPE} = 800 \text{ J kg}^{-1}$  cases and  $14 \text{ m s}^{-1}$  for the  $\text{CAPE} = 2000 \text{ J kg}^{-1}$  cases. Increasing  $V$  to  $14 \text{ m s}^{-1}$  for the larger CAPE cases was necessary to keep the bulk Richardson number within the supercell regime for all of the buoyancy and wind shear profile shapes employed. The resulting wind profiles for  $V = 12$  are illustrated in Fig. 1c for the curved hodograph cases, and in Fig. 1d for the straight hodograph cases. With the two different CAPE regimes and two types of hodographs being employed, we obtain four separate matrices of nine simulations each. We also performed simulations at  $\text{CAPE} = 2000 \text{ J kg}^{-1}$  with  $V = 12$ , but because their weak shear cases feature bulk Richardson number values slightly outside the supercell regime, the results are mentioned only briefly in the discussion.

Our simulations are conducted using the Klemp–Wilhelmson model (Klemp and Wilhelmson 1978; Wilhelmson and Chen 1982) on a  $50 \text{ km} \times 50 \text{ km}$  domain  $20 \text{ km}$  deep. Horizontal resolution of the grid mesh is  $500 \text{ m}$ . A stretched mesh is employed in the vertical, with  $250\text{-m}$  resolution at the bottom, increasing steadily to  $750 \text{ m}$  at the top. All integrations are carried out to  $2 \text{ h}$  of simulated time, using a large time step of  $4.0 \text{ s}$ . Convection is launched with initial thermal perturbations similar in spatial distribution to those described in Klemp and Wilhelmson (1978), but with amplitudes of  $4.0 \text{ K}$  for the small CAPE simulations and  $2.0 \text{ K}$  for the large CAPE simulations; horizontal and vertical radii of  $12$  and  $2.5 \text{ km}$ , respectively; and centers at  $z = 0$ . These thermal amplitudes are approximately the smallest that could be used to create convection that persists into the second hour in all simulations within the two CAPE regimes, given the prescribed shears. All other model parameters are assigned identical values across all the simulations, except the prescribed minimum value of the second-order vertical mixing coefficient, which was set to  $16 \text{ m}^2 \text{ s}^{-1}$  within the two small CAPE simulation matrices, and  $50 \text{ m}^2 \text{ s}^{-1}$  for the four large CAPE matrices. These changes in mixing coefficient were helpful in suppressing numerical instability in simulations where strong updrafts were expected and in preventing suppression of storms in cases where weak updrafts were expected. The straight hodograph simulations are conducted using an axis of symmetry through the initial thermal bubble, and only the right halves of the symmetric convection field are simulated. The Coriolis parameter is set to zero in all our simulations.

No ice phase microphysics are included in the present



model. The lack of ice physics is expected to have its strongest impact on features such as storm-top height, downdraft and outflow structure, and possibly surface vorticity (Jewett et al. 1990; Straka et al. 1993). We have included comments below wherever we feel caution is advised in interpreting our data. However, test simulations were also conducted on a subsample of our starting environments using a model with full ice microphysics, which confirm the general validity of our findings (C. Cohen 1999, personal communication).

### 3. Results

In describing the simulation results, we employ a nomenclature for each matrix that contains information about the bulk CAPE (e.g., E0800 for the CAPE = 800 J kg<sup>-1</sup> simulations), and the hodograph trace (e.g., V12C for a hodograph trace radius of 12 m s<sup>-1</sup> having semicircular curvature, or V14S for one with a 14 m s<sup>-1</sup> radius unfolded into a straight line). Thus a matrix where all the simulations were initiated in environments having CAPE = 800 J kg<sup>-1</sup> and a 12 m s<sup>-1</sup> curved hodograph would be designated by the shorthand name E0800-V12C. Using this nomenclature, we will first describe the E0800-V12C and E0800-V12S simulation matrices. We conclude by describing the results of the two enhanced CAPE, enhanced shear simulation series, E2000-V14C and E2000-V14S.

Although we conducted nine simulations within each of the matrices, we present here only the results from the corners of each matrix. Our results suggest that storm intensity parameters in the other cells of the matrices can, to within the small degree of expected variability between individual simulations, be inferred by interpolating between the corner cells of the simulation matrices. The essence of our results thus lies in the corners of the matrices. Results will thus be presented in 2 × 2 matrices of horizontal cross section maps, in 2 × 2 matrices of summarized tabular data, and in 2 × 2 matrices of time series plots of peak values of selected storm intensity parameters.

#### a. E0800-V12 simulations

Results from E0800-V12C and E0800-V12S are summarized in Figs. 3 and 4, which depict maps of the fields of  $w$  at  $z = 1.71$ -km altitude (contours), rainwater mixing ratio  $q_r$  at  $z = 0.127$  km, and horizontal storm-relative wind vectors at  $z = 0.127$  km. The plots are constructed using data from times of characteristic mature storm structure during the second hour of the simulations, in 20 km × 20 km subdomains roughly centered on the principal storm of interest. These parameters are shown in order to convey in a simple manner some sense of storm structure and size, particularly the relationship between updraft structure aloft and inflow-outflow structure at the surface.

In describing the character of our simulated storms,

we will attempt to follow the general guidelines given by other authors who have discussed the spectrum of supercell morphology (Doswell and Burgess 1993; Moller et al. 1994). In particular, we consider any storm containing a rotating updraft that persists into the second hour of the simulation to be a supercell; rotation must be persistent through a sizeable depth of the storm, with peak vertical vorticity regularly exceeding 0.01 s<sup>-1</sup>. Storms with these rotating updrafts also tend to display hook echo configurations embracing inflow notches in their low-level precipitation fields. Supercells having relatively little precipitation footprint in the rear-flank region (i.e., within the hook echo and along the flanking line) are termed classic (CL), whereas those showing more comparable amounts of precipitation in both the forward and rear flank regions are termed heavy precipitation (HP). A third type of supercell, the so-called low-precipitation type (LP) does not appear in our results. The assessment of supercell type is somewhat subjective, inasmuch as no quantitative index of supercell morphology has yet gained acceptance.

The maps for E0800-V12C (Fig. 3) show considerable variety in the configurations of storm updraft, precipitation, and surface outflow. The updrafts are much stronger, larger, and more numerous in the two large-lapse rate simulations ( $Z_b = 2.5$  km) than for those having small environmental lapse rates ( $Z_b = 5.5$  km). The surface precipitation shafts are also either larger and more intense or more numerous for the  $Z_b = 2.5$  km cases, but when the low-level shear is enhanced ( $Z_v = 2.5$  km), the heaviest precipitation is displaced farther downstream from the updraft. The surface outflow is also much more fully developed in the two large-lapse rate cases ( $Z_b = 2.5$  km). In general, it appears that the large-lapse rate, strong shear case ( $Z_b = Z_v = 2.5$  km) represents a shallow but intense CL supercell storm (Doswell and Burgess 1993; Moller et al. 1994), whereas the other cases appear to be smaller and weaker versions of supercells. The storm in case  $Z_b = 5.5$  km,  $Z_v = 2.5$  km is very small and weakens substantially during the second hour. However, despite its somewhat transient character, it does display peak updraft-vorticity correlations as large as 0.85 prior to weakening. This is an example of the low-level shear actually being too strong relative to the low-level buoyancy to sustain a long-lived supercell.

For the E0800-V12S cases, the maps in Fig. 4 show at least as much variety as Fig. 3. The updrafts and precipitation shafts are again larger, more intense and more numerous when the low-level lapse rates are enhanced ( $Z_b = 2.5$  km). As in the curved hodograph regime, the  $Z_b = Z_v = 2.5$  km case produces the largest and strongest CL supercell. For the large-lapse rate, weak shear case  $Z_b = 2.5$  km,  $Z_v = 5.5$  km, the surface outflow propagates rapidly toward positive  $x$  and  $y$ , which, in combination with the weakness of the low-level ambient shear, causes the updrafts to tilt backward relative to their propagation direction. At the same time,

CAPE=0800,  $V=12$ , CURVED, LCL=0.5km  
HORIZONTAL SECTIONS: W, QR, VECT

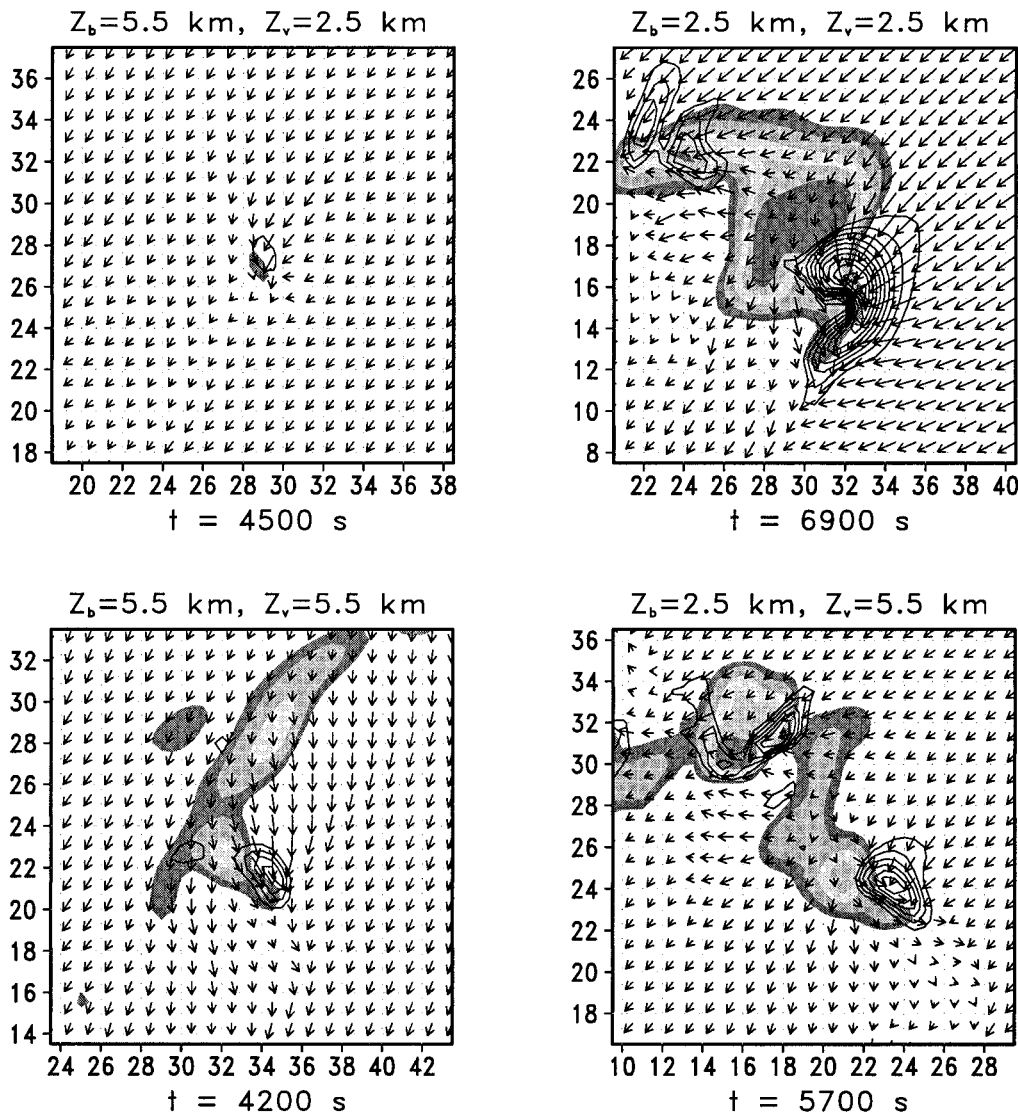


FIG. 3. Maps of simulated updraft velocity  $w$  at  $z = 1.71$  km (contoured at  $2 \text{ m s}^{-1}$  intervals), rainwater mixing ratio  $q_r$  at  $z = 0.127$  km (shaded starting at 0.5, 1.0, 2.0, 3.0, and  $4.0 \text{ g kg}^{-1}$  values), and horizontal storm-relative wind vectors (every other vector removed) at  $z = 0.127$  km for the E0800-V12C simulations. Coordinates relative to the full simulation domain are marked at 2-km intervals along the sides of the plots. Vectors are scaled so that a length of 1 km on the plots corresponds to a wind speed of  $12.5 \text{ m s}^{-1}$ . All plots are taken from the second hour of the simulated storms at selected times (see markings beneath each panel) deemed representative of mature storm structure.

these factors apparently allow the leading edge of the storm outflow to regulate storm updraft development. This produces a surface precipitation pattern much different from that of the  $Z_b = Z_v = 2.5$  km CL supercell, and it suggests HP supercell, almost multicell, morphology. Indeed, in this storm, the mature principal updraft and mesocyclone are located in Fig. 4 near  $(x = 12, y = 26)$ , while a new supercell updraft is building at  $(x = 19, y = 24)$ , on the main storm's flank. The

storm in the small-lapse rate, weak shear case  $Z_b = Z_v = 5.5$  km appears to be a small CL supercell. The storm in the small-lapse rate, strong shear case  $Z_b = 5.5$  km,  $Z_v = 2.5$  km is, like its counterpart in the curved hodograph cases, so small and weak (peak maximum updraft only  $11 \text{ m s}^{-1}$ ) that it is also considered insignificant. It is, however, slightly stronger and more persistent than its curved hodograph counterpart.

Figures 5a and 5c show several relevant environ-

CAPE=0800, V=12, STRAIGHT, LCL=0.5km  
HORIZONTAL SECTIONS: W, QR, VECT

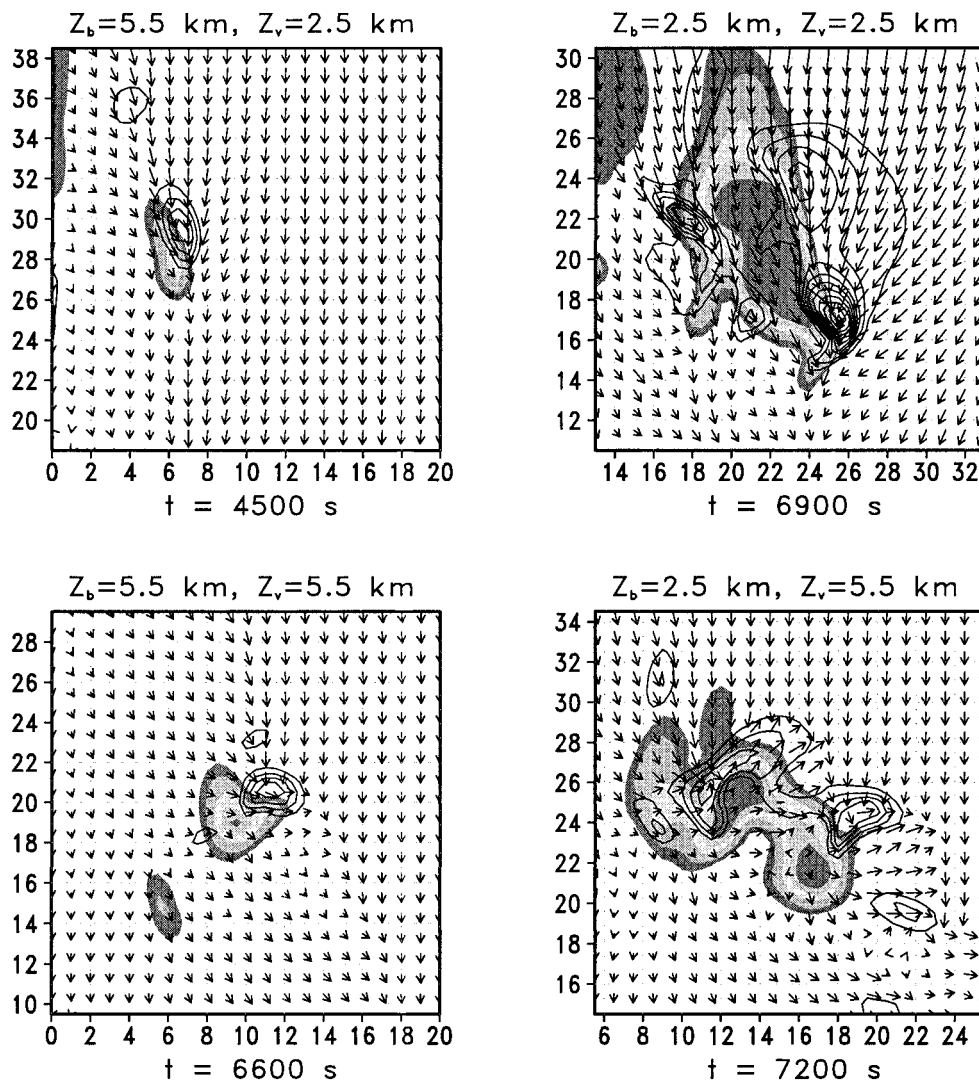


FIG. 4. As in Fig. 3, but for the E0800-V12S simulations.

mental parameters for both hodograph regimes in these small CAPE cases. Parameters shown include theoretical parcel lifted index, LI, at 500 hPa (units are  $^{\circ}\text{C}$ ); theoretical peak parcel potential temperature excess, TMAX, relative to the environment (units are K); bulk Richardson number, BRN (Weisman and Klemp 1982); 0–6-km shear, BSHR, used in the bulk Richardson number calculation (BRN shear; units are  $\text{m s}^{-1}$ ); integrated 0–3-km storm-relative helicity density, HEL (Lilly 1986; Davies-Jones et al. 1990; units are  $\text{J kg}^{-1}$ ); characteristic  $x$  and  $y$  components of ground-relative storm cell motion, MOT, for the dominant cell of interest during the second hour of simulated time (units are  $\text{m s}^{-1}$ ); and storm-relative environmental inflow, INFL ( $\text{m s}^{-1}$ ),

at the lowest model level. The computed values of INFL and 0–3-km HEL are relative to the characteristic storm cell motions defined by MOT. Although the parameters INFL and HEL are dependent on the motion of the simulated storms, they must often be forecast operationally from prestorm environmental data and are thus listed here as environmental parameters for convenience.

The environmental buoyancy parameters LI and TMAX are small for the E0800-V12 simulations, as expected when CAPE is small. All values of LI are near  $-2.3^{\circ}\text{C}$ , regardless of which buoyancy profile is examined. This is because for  $Z_b = 5.5$  km the peak parcel buoyancy TMAX is only  $2.3^{\circ}\text{C}$  and is achieved at a

$$\text{CAPE} = 800 \text{ J/kg}, V = 12 \text{ m/s}$$

(a) ENVIRONMENTAL PARAMETERS (CURVED HODOGRAPHS)		(b) SIMULATED STORM PARAMETERS (CURVED HODOGRAPHS)	
$Z_b = 5.5\text{km}$	$Z_b = 2.5\text{km}$	$Z_b = 5.5\text{km}$	$Z_b = 2.5\text{km}$
LI : -2.3 TMAX: 2.3 BRN : 7.3 BSHR: 14.7 HEL : 178 MOT : -8.6,-0.1 INFL: 5.1	LI : -2.2 TMAX: 3.8 BRN : 7.3 BSHR: 14.7 HEL : 263 MOT : -1.5,2.4 INFL: 11.9	TYPE: S-TR WMAX: 8 VORT: 216,153 TOP : 1.9 TMIN: -2.1 ZWMX: 0.8 CORR: 0.37,0.85	TYPE: S-CL WMAX: 30 VORT: 370,354 TOP : 8.3 TMIN: -5.2 ZWMX: 3.2 CORR: 0.68,0.92
LI : -2.3 TMAX: 2.3 BRN : 16.9 BSHR: 9.7 HEL : 62 MOT : -8.2,1.6 INFL: 5.1	LI : -2.2 TMAX: 3.8 BRN : 16.9 BSHR: 9.7 HEL : 67 MOT : -6.6,4.3 INFL: 8.2	TYPE: S-CL WMAX: 11 VORT: 172,122 TOP : 8.3 TMIN: -3.4 ZWMX: 1.4 CORR: 0.63,0.72	TYPE: S-CL WMAX: 19 VORT: 215,234 TOP : 5.4 TMIN: -4.9 ZWMX: 2.4 CORR: 0.51,0.78

(c) ENVIRONMENTAL PARAMETERS (STRAIGHT HODOGRAPHS)		(d) SIMULATED STORM PARAMETERS (STRAIGHT HODOGRAPHS)	
$Z_b = 5.5\text{km}$	$Z_b = 2.5\text{km}$	$Z_b = 5.5\text{km}$	$Z_b = 2.5\text{km}$
LI : -2.3 TMAX: 2.3 BRN : 4.5 BSHR: 18.8 HEL : 68 MOT : 2.5,2.5 INFL: 7.4	LI : -2.2 TMAX: 3.8 BRN : 4.5 BSHR: 18.8 HEL : 153 MOT : 5.7,7.2 INFL: 13.0	TYPE: S-TR WMAX: 9 VORT: 193, 60 TOP : 3.3 TMIN: -2.4 ZWMX: 1.5 CORR: 0.48,0.74	TYPE: S-CL WMAX: 24 VORT: 347,148 TOP : 9.3 TMIN: -6.0 ZWMX: 2.7 CORR: 0.58,0.77
LI : -2.3 TMAX: 2.3 BRN : 14.2 BSHR: 10.6 HEL : 34 MOT : 2.4,4.5 INFL: 6.9	LI : -2.2 TMAX: 3.8 BRN : 14.2 BSHR: 10.6 HEL : 45 MOT : 3.1,7.3 INFL: 9.8	TYPE: S-CL WMAX: 11 VORT: 150,154 TOP : 10.4 TMIN: -4.3 ZWMX: 2.5 CORR: 0.52,0.82	TYPE: S-HP WMAX: 18 VORT: 255,344 TOP : 7.8 TMIN: -6.8 ZWMX: 3.2 CORR: 0.31,0.49

FIG. 5. Environmental and storm parameters for E0800-V12C cases [(a),(b)] and E0800-V12S cases [(c),(d)]. Coded labels are described in the text.

level very close to 500 hPa (where LI is measured), while for  $Z_b = 2.5$  km, the peak parcel buoyancy TMAX is almost  $4^\circ\text{C}$ , but occurs some 3 km below the 500-hPa level, so that only a little more than half of this buoyancy is present at the level where LI is computed. BRN values suggest the potential for supercell convection for all cases. BRN shears BSHR are slightly smaller

in the E0800-V12C cases than for their counterparts in E0800-V12S, because hodograph curvature reduces the vector differences in velocity between any two levels relative to a straight hodograph having the same shear profile. The storm-relative environmental helicity HEL varies sharply among the various storms in E0800-V12, but always increases as both  $Z_b$  and  $Z_v$  decrease. The



largest HEL,  $263 \text{ J kg}^{-1}$ , occurs for case  $Z_b = Z_v = 2.5 \text{ km}$  in the E0800-V12C matrix. The behavior of storm cell motions MOT and of low-level storm inflow INFL will be discussed separately later for all simulations.

Figures 5b and 5d also display values of some important descriptive storm intensity parameters seen in the simulated storms during the second hour of the simulations. These parameters are TYPE, subjectively assessed characteristic storm morphology (M = multicell, S = supercell, CL = classic, HP = high precipitation, TR = transient, HY = hybrid); WMAX, peak updraft speed  $w_{\text{max}}$ ,  $\text{m s}^{-1}$ ; VORT, consisting of two parameters, VMID and VSFC, peak midlevel and near-surface vertical vorticity  $\zeta_{\text{mid}}$  and  $\zeta_{\text{sfc}}$ , respectively, with units  $10^{-4} \text{ s}^{-1}$ ; TOP, the altitude of highest storm top, in units of km; ZWMX, the altitude of the time-averaged level of maximum updraft, also in units of km; TMIN, amplitude of peak near-surface potential temperature deficits  $\theta'_{\text{min}}$ , K, in the storm outflows; and CORR, the minimum and maximum values in the time series of peak values in the profiles of the linear correlation coefficients between fields of vertical velocity  $w$  and vorticity  $\zeta$ . The near-surface parameters VSFC and TMIN are obtained from data at the lowest model thermodynamic level, which lies at  $z = 127 \text{ m}$ . All the variables are evaluated using model data limited spatially to migratory  $10 \text{ km} \times 10 \text{ km}$  subdomains containing the subjectively determined principal storm of interest during the second hour of the simulations. Also, all parameters except WMAX are derived from the simulation fields saved every 300 s; WMAX is evaluated from supplementary model output listings obtained every 12 s of simulated time.

Inspection of the matrices of Fig. 5 shows clearly that, despite the above caveats, there exist obvious differences in many important storm intensity parameters within each matrix. However, differences in parameters such as WMAX between curved and straight hodograph cases having similar combinations of shape parameter values are generally smaller. Note that for the curved hodograph case  $Z_b = 5.5 \text{ km}$ ,  $Z_v = 2.5 \text{ km}$ , corresponding to small low-level lapse rates and strong low-level shear, the peak updraft WMAX is only  $8 \text{ m s}^{-1}$ , while for the case  $Z_b = Z_v = 2.5 \text{ km}$ , featuring large lapse rates and shear coexisting in a shallow layer near cloud base, the corresponding value is  $30 \text{ m s}^{-1}$ . Because the environmental CAPE is  $800 \text{ J kg}^{-1}$ , an undiluted updraft could attain a peak speed of  $40 \text{ m s}^{-1}$  according to parcel theory. Thus the overturning efficiency (McCaul and Weisman 1996) of the latter case reaches 0.75, while that of the former is only 0.20. Results for the corresponding elements of the straight hodograph matrix show differences almost equally dramatic.

The other cases in E0800-V12 exhibit peak updraft intensities WMAX generally intermediate between the extreme cases described in the previous paragraph. It is noteworthy that for both the curved and straight hodograph regimes, the small low-level lapse rate ( $Z_b = 5.5 \text{ km}$ ), strong low-level shear ( $Z_v = 2.5 \text{ km}$ ) cases

show smaller updraft strengths even than those of the ( $Z_b = Z_v = 5.5 \text{ km}$ ) cases. For both these small-lapse rate, strong shear storms, we find that the environments are only marginally able to support convection continuing into the second hour of the simulations, given our model initialization specifications. In all cases, enhancement of the low-level shear for a given buoyancy profile causes the simulated storms to build to peak intensity more slowly (Figs. 4, 5). This is consistent with findings of many prior investigations (e.g., Schlesinger 1978; Weisman and Klemp 1982).

As a mechanism of updraft enhancement, the impact of the buoyancy stratification is generally more important than that of the shear stratification, at least for the E0800-V12C and E0800-V12S experiments. As the low-level buoyancy increases, WMAX increases for the weak shear cases  $Z_v = 5.5 \text{ km}$  by approximately 65%–75% for both the curved and straight hodograph matrices. For the strong shear cases  $Z_v = 2.5 \text{ km}$ , there is even more sensitivity to the buoyancy stratification, with updraft enhancements ranging from roughly 170% to nearly 270% as low-level buoyancy increases. The importance of the buoyancy stratification is confirmed by means of a series of zero-wind simulations (not included in the tables), where it is found that the peak updraft for the  $Z_b = 2.5 \text{ km}$  case is more than  $37 \text{ m s}^{-1}$ , roughly 50% larger than the  $25 \text{ m s}^{-1}$  value for the case  $Z_b = 5.5 \text{ km}$ .

In the E0800-V12 simulations, peak storm midlevel vorticity VMID appears to correlate better with updraft intensity WMAX than with either the low-level lapse rate or low-level vertical shear alone. The behavior of the near-surface peak vorticity VSFC is, however, more variable. For both the curved and straight hodograph matrices, intramatrix intercomparisons reveal that VSFC generally increases with increasing cold pool temperature deficits -TMIN, although within any single simulation, this correlation is often obscured by short-term storm dynamical fluctuations. The dependence of VSFC on the low-level shear differs, however, for the curved and straight hodograph regimes, with stronger shears associated with stronger peak VSFC when hodographs are curved, but with weaker peak VSFC when hodographs are straight. We find, however, that VSFC is highly sensitive to the details of the evolution of a storm's low-level outflow, and can show sudden increases that may not always be sampled adequately during a 2-h simulation period. Nevertheless, the positive impact that enhancement of the surface cold pool strength appears to have on the near-surface vertical vorticity in these simulations is evident and is reminiscent of the results presented by McCaul and Weisman (1996) in their simulations of hurricane-spawned severe storms.

The two height parameters, TOP and ZWMX, are quite variable across the E0800-V12 simulations. As will be seen in other cases presented below, storm updraft tops TOP tend to be largest when both the buoy-

ancy and wind-scale altitudes are simultaneously at their largest. In E0800-V12C, however, the  $Z_b = Z_v = 2.5$  km storm is so intense that its TOP matches that of the  $Z_b = Z_v = 5.5$  km storm. TOP for the small, transient storms found in the small-lapse rate, strong shear environments ( $Z_b = 5.5$  km,  $Z_v = 2.5$  km) is extremely shallow. The altitude of maximum updraft ZWMX is greatest for the storms occurring in environments with large low-level lapse rates, and it appears to be considerably larger than the depth of the cold pools in those storms.

In both the small CAPE matrices, the amplitudes of the cold pool temperature deficits -TMIN are roughly correlated with the maximum parcel buoyancy TMAX, which is inversely related to the value of  $Z_b$ . Although it is customary to assess the likely value of peak cold pool temperature deficits by comparing the minimum ambient equivalent potential temperatures  $\theta_e$  at midlevels with those at cloud base, we find here that, because we have not allowed any variations in the ambient profiles of relative humidity, TMAX is a good surrogate for these  $\theta_e$  differences. This explains the dependence of -TMIN on the ambient thermodynamic profile shapes.

For the small lapse rate cases, there is also an apparent negative correlation between -TMIN and the strength of the low-level vertical shear. This inverse relationship may derive from the fact that stronger shears and smaller buoyancies promote excessive updraft tilt, which reduces concentrations of precipitation and water loading, minimizes evaporative cooling and downdrafts, and encourages premature storm dissipation. Under these conditions, even the modest maximum potential TMIN deficits implied by the thermodynamic stratification cannot be realized.

Also shown in Fig. 5 are the minima and maxima in the second-hour time series of peak values of the profiles of linear correlation coefficient CORR between the fields of vertical velocity  $w$  and vertical vorticity  $\zeta$ . In each storm, the maximum CORR peak values approach or exceed 0.5 and are large enough to suggest likely supercell structure. In fact, many of the storms exhibit minimum CORR peak values near this threshold. Indeed, our subjectively assigned storm morphology parameters TYPE tend to agree with this, although there are some differences in storm structural details.

Time histories of selected storm parameters WMAX, VMID, VSFC, and -TMIN for the small CAPE storms are shown in Fig. 6 for the curved hodograph cases and in Fig. 7 for the straight hodograph cases. These time histories are based on simulation data saved at 300-s intervals. The figures indicate that ratios of VMID and VSFC are rather close to unity in all the simulations, except in the two  $Z_v = 2.5$  km straight hodograph cases, where VSFC is always smaller than VMID. The evolution of VMID tends to follow that of WMAX. VSFC exhibits considerable temporal and proportional variability in some of the simulations, particularly the case  $Z_b = Z_v = 2.5$  km with curved hodograph. VMID, on

the other hand, shows less proportional temporal variability than does VSFC.

#### b. E2000-V14 simulations

The storms described in the previous section all tended to be invigorated by enhancement of the low-level environmental lapse rates. On the other hand, the storms either weakened, for the small-lapse rate cases, or strengthened, for the large-lapse rate cases, in response to enhanced low-level vertical shear. We now examine how storms respond to an increase in bulk CAPE and then to an increase in bulk shear.

Increasing the CAPE from 800 to 2000 J kg<sup>-1</sup>, without any increase in bulk shear, produces environments having generally larger BRN values, which moves a portion of the environmental parameter space into the multicell regime. In order to create environments with smaller BRNs so that the simulations remained nominally in the supercell regime, the hodograph trace radius was expanded to 14 m s<sup>-1</sup>. This produced a simulation series called E2000-V14. However, simulations were also conducted for E2000-V12 environments (not shown) to allow for a more direct comparison with the E0800-V12 simulations. As expected, the E2000-V12 storms were generally larger and more intense than their counterparts in E0800-V12. Not surprisingly, some of the E2000-V12 storms displayed more multicellular behavior compared with E0800-V12 and thus could not readily be compared dynamically to the E0800-V12 storms. On the other hand, it was found that the differences between the E2000-V12 and the E2000-V14 storm morphologies for the cases with BRNs within the supercell regime were not significant.

Results from the corners of these E2000-V14C and E2000-V14S simulation matrices are presented in Figs. 8–12. The simulations in these figures feature all possible combinations of buoyancy and wind profile-scale altitudes  $Z_b = 7.1$  or 4.1 km and  $Z_v = 7.1$  or 4.1 km. The figures confirm that most of the storms simulated in the E2000-V14 matrices are considerably more intense than their counterparts with similar buoyancy and wind-scale altitudes in E0800-V12. They are also slightly more intense than their counterparts in E2000-V12 (not shown).

The strong shear ( $Z_v = 4.1$  km) cases in E2000-V14C (Figs. 8, 9) represent particularly intense and well-developed forms of supercell convection. Both these CL supercell cases exhibit cyclonically curved updraft–downdraft couplets, with the  $Z_b = 4.1$  km case featuring peak surface vorticity values larger than 0.04 s<sup>-1</sup>. Its counterpart in E2000-V14S assumes the form of a short line of cells, with the principal storm an HP supercell having peak surface vorticity VSFC approaching 0.04 s<sup>-1</sup>. In many cases, the convection tends to be organized by an intense surface outflow boundary. This is especially evident when the hodographs are straight. In most

CAPE=0800,  $V=12$ , CURVED, LCL=0.5km  
TIME SERIES: WMAX, VMID, VSFC, -TMIN

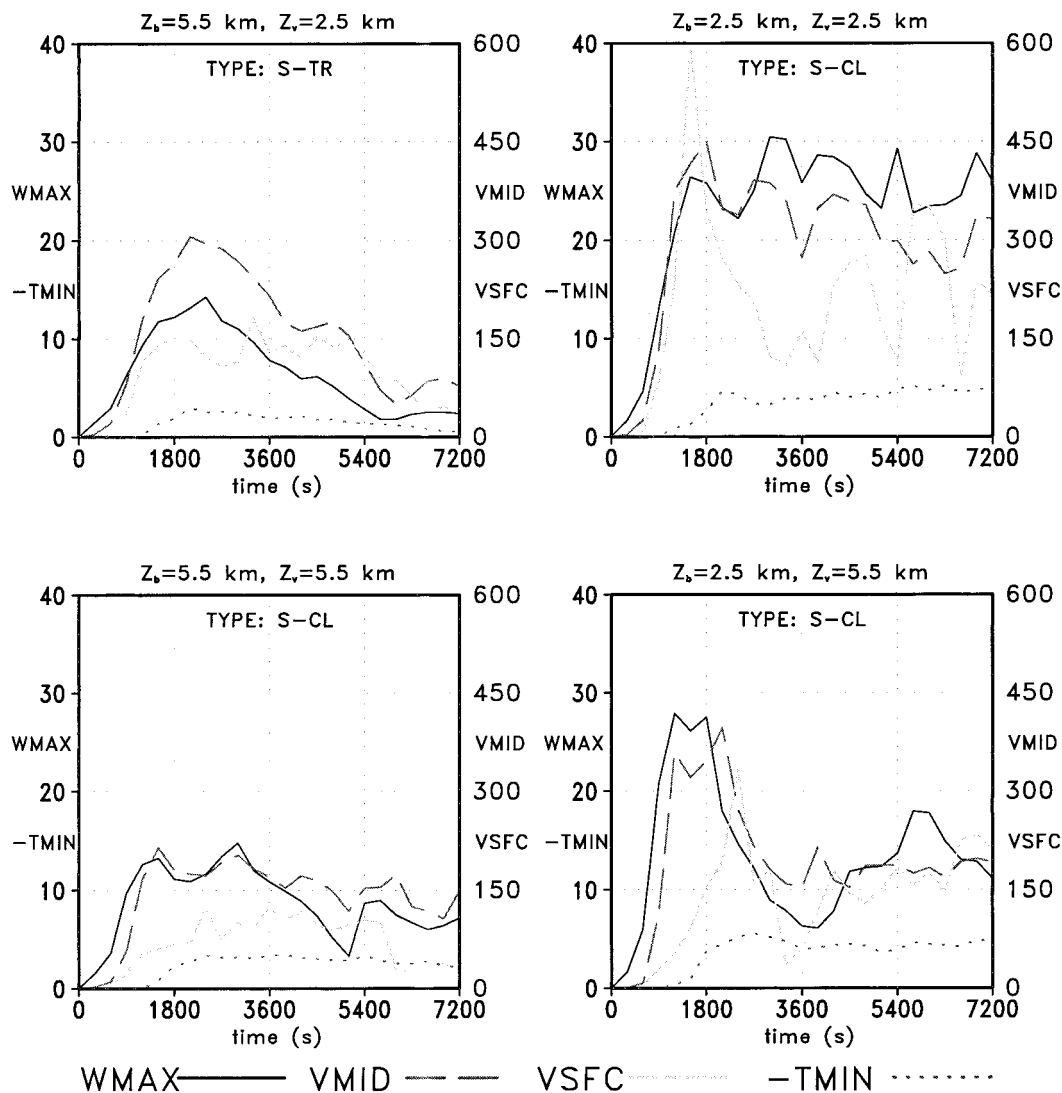


FIG. 6. Evolution of selected storm peak parameters WMAX, VMID, VSFC, and -TMIN vs time (s) for the E0800-V12C simulations. Scales on the left side of each graph refer to WMAX and -TMIN, while those on the right refer to VMID and VSFC. The peak parameters are defined in the text.

cases from E2000-V14S, individual storm cells are able to propagate at speeds that allow them to establish themselves as persistent entities moving with the outflow boundary. However, something quite different occurs with the weak shear ( $Z_v = 7.1$  km) storm cells in the straight hodograph matrix. For these simulations, the storm cells are unable to propagate fast enough in the  $x$  direction to keep up with the rapidly spreading outflow boundary.

The environmental parameters from E2000-V14 (Figs. 10a,c) confirm larger amplitudes for the buoyancy parameters LI and TMAX, as compared to those in Figs.

5a,c. Furthermore, the buoyancy profile shapes for the E2000-V14 simulations show less tendency for TMAX to vary with  $Z_b$ , as compared to the E0800-V12 environments. Because of the large increase in CAPE and only small increase in bulk shear, the bulk Richardson numbers BRN show the expected increases relative to those in E0800-V12, with the weaker shear cases now growing to magnitudes that lie close to the multicell regime. As before, the helicity parameter HEL tends to increase as both the buoyancy and wind-scale altitudes  $Z_b$  and  $Z_v$  decrease. However, the largest HEL values in E2000-V14 ( $177 \text{ J kg}^{-1}$  for  $Z_b = Z_v = 4.1$  km in

CAPE=0800, V=12, STRAIGHT, LCL=0.5km  
TIME SERIES: WMAX, VMID, VSFC, -TMIN

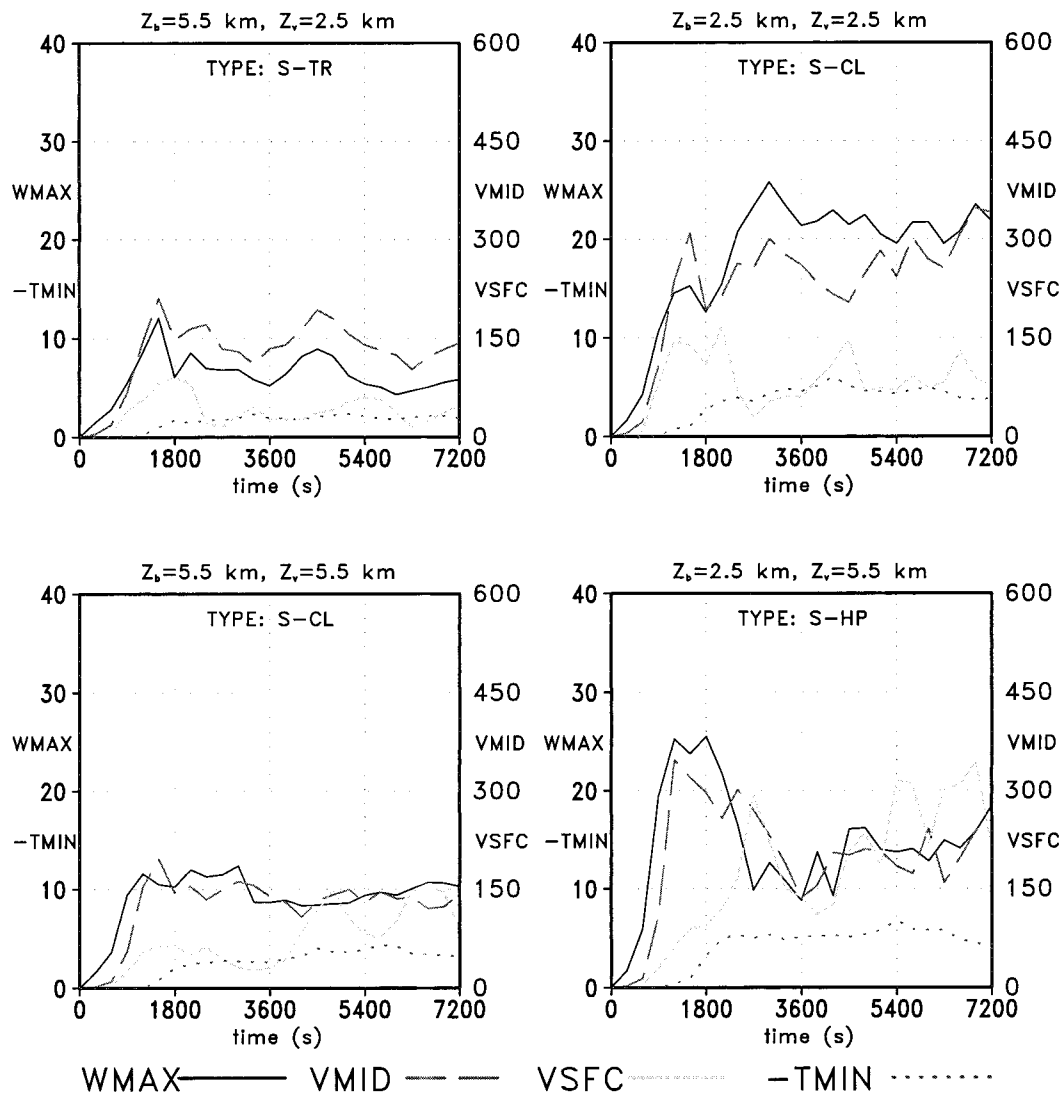


FIG. 7. As in Fig. 6, but for the E0800-V12S simulations.

E2000-V14C) are still smaller than the  $263 \text{ J kg}^{-1}$  seen for case  $Z_b = Z_v = 2.5 \text{ km}$  in E0800-V12C.

As with Fig. 5, the simulated storm parameters in Fig. 10 also show differences in most cases as  $Z_b$  and  $Z_v$  vary, but the relative differences are generally smaller than in the small CAPE simulations. In Fig. 10, the peak updraft speeds WMAX still show increases with both decreasing  $Z_b$  and  $Z_v$ , as in Fig. 5. In Fig. 10, however, the largest relative increases in WMAX are only roughly 50%–100%, as opposed to the 200% or more seen in Fig. 5. For WMAX, the variations in peak amplitude between the simulations continue to lie in a range that appears to be statistically significant.

Like WMAX, the peak midlevel vorticity VMID in Fig. 10 tends to exhibit somewhat less sensitivity to both the buoyancy and wind-scale altitudes  $Z_b$  and  $Z_v$  than that seen in the small CAPE simulations. The largest relative variations of VMID within each matrix are about 50%–80%. Unlike WMAX, where the smallest values are consistently found in the cases having both large  $Z_b$  (small low-level lapse rates) and large  $Z_v$  (weak low-level shears), the smallest values of VMID tend to occur when  $Z_v$  is large (weak low-level shears) and  $Z_b$  small (large low-level lapse rates). On the other hand, the peak surface vorticity VSFC in Fig. 10 tends to be largest when  $Z_b$  and  $Z_v$  are both large or both small.



CAPE=2000,  $V=14$ , CURVED, LCL=0.5km  
HORIZONTAL SECTIONS: W, QR, VECT

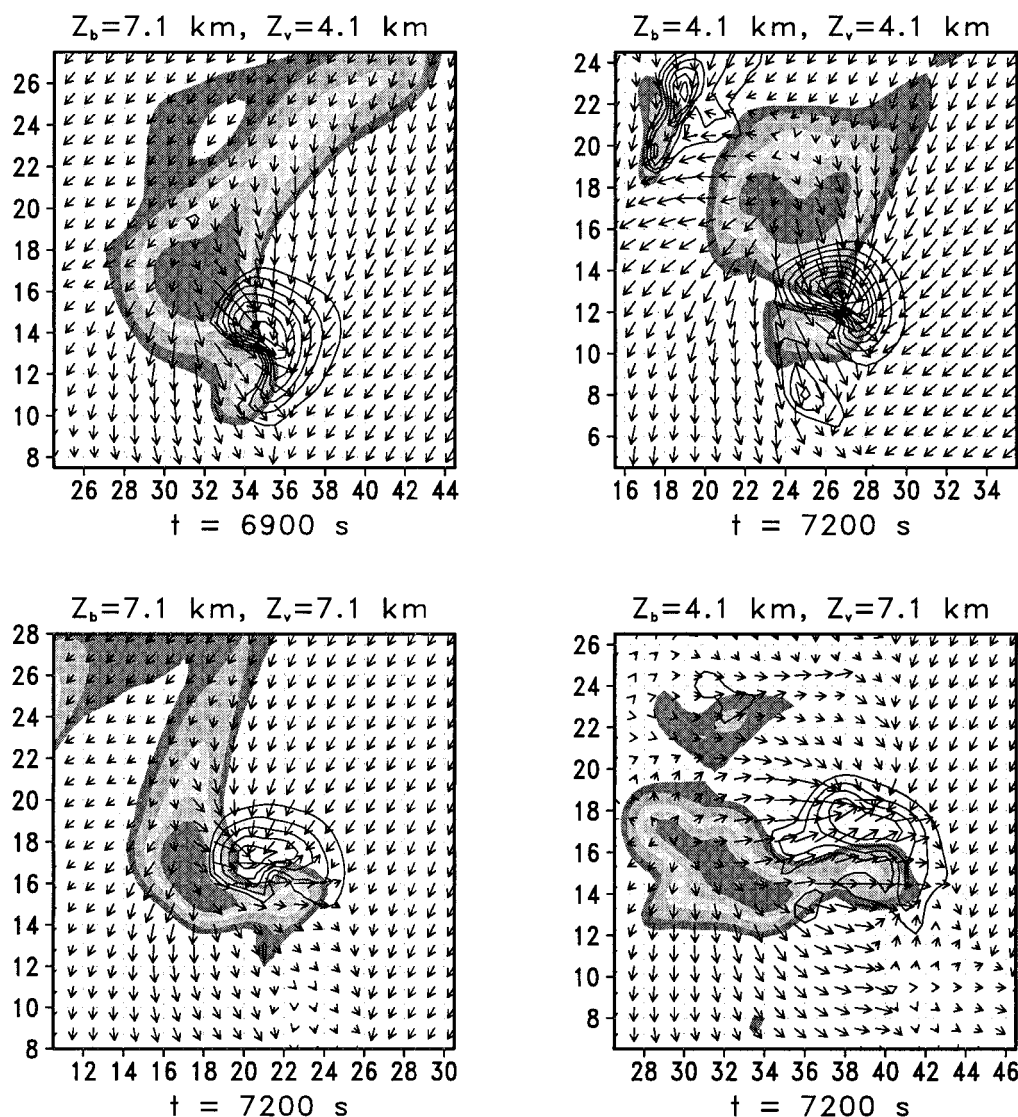


FIG. 8. As in Fig. 3, but for E2000-V14C simulations.

The maximum differences in VSFC are on the order of 100%, but because of the limitations of the simulations with respect to the representation of cloud and precipitation microphysics, the significance of these variations in VSFC remains uncertain.

The storms in E2000-V14 are generally larger and deeper than those in E0800-V12. The TOP parameter indicates storm tops above 13 km for the small low-level lapse rate, weak low-level shear ( $Z_b = Z_v = 7.1$  km) cases, with lower maximum tops in the large low-level lapse rate cases. The smallest values of TOP tend to occur with the large low-level lapse rate, weak low-level shear storms ( $Z_b = 4.1$  km,  $Z_v = 7.1$  km). Al-

titudes ZWMX of maximum updraft speed generally show little variability, always lying between 3.5 and 4.5 km AGL.

In both E2000-V14 matrices, surface cold pool intensity, as reflected by the value of -TMIN, grows with decreasing values of buoyancy scale altitude (i.e., increasing low-level lapse rate) but shows negligible sensitivity to the wind-scale altitude (low-level shear). The values of -TMIN in Fig. 10 are considerably larger in amplitude than those in Fig. 5, as expected in view of the differences in CAPE and TMAX. The  $w$ - $\zeta$  correlations are large in all cases and are generally larger for the curved hodograph cases than for the straight.

CAPE=2000,  $V=14$ , STRAIGHT, LCL=0.5km  
HORIZONTAL SECTIONS: W, QR, VECT

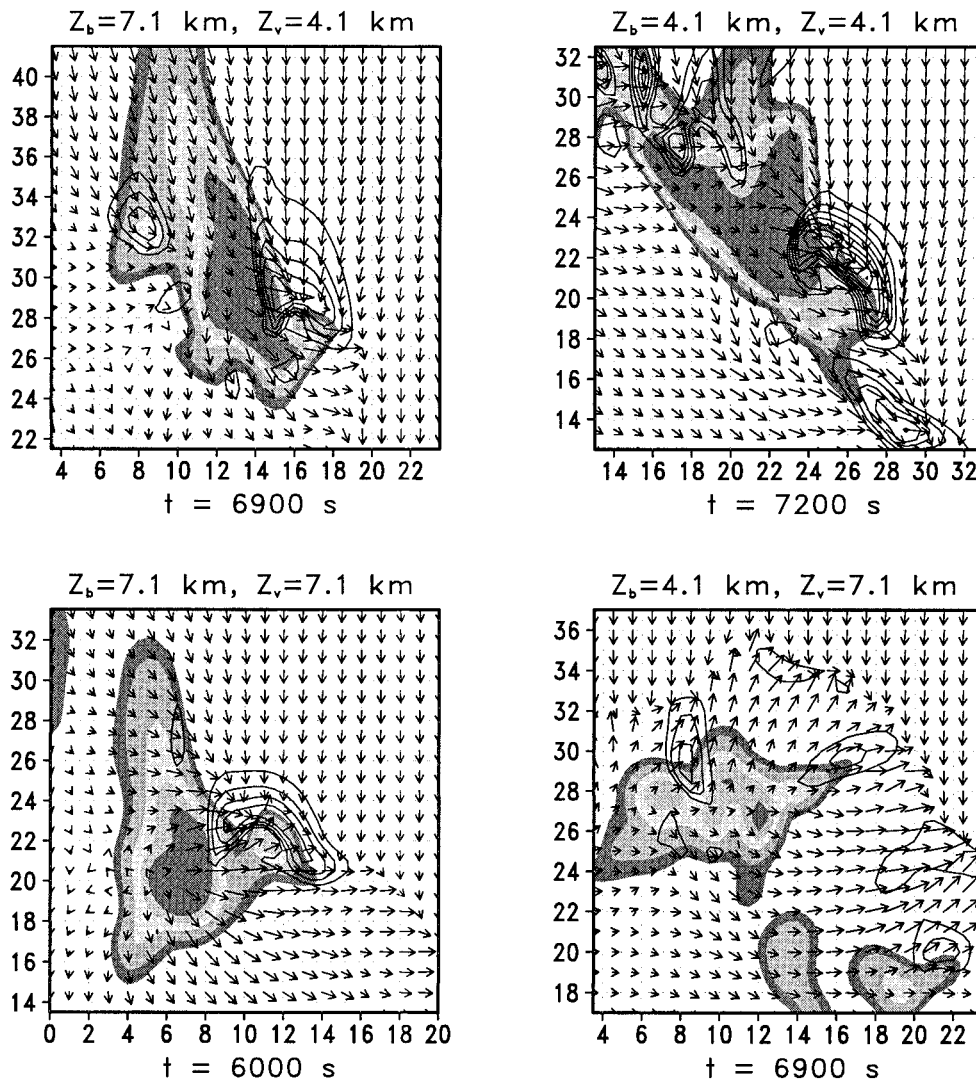


FIG. 9. As in Fig. 4, but for E2000-V14S simulations.

Upon close study, interpolation of the Fig. 10 WMAX values reveals that the peak updrafts in the E2000-V14 matrices at  $Z_b = Z_v = 5.5$  km are stronger than their  $Z_b = Z_v = 5.5$  km counterparts in E0800-V12 (Fig. 5). This is not surprising in view of the fact that CAPE is much larger for the storms described in Fig. 10. However, it is noteworthy that the WMAX for the  $Z_b = Z_v = 2.5$  km case in E0800-V14C,  $30 \text{ m s}^{-1}$ , is almost as large as the largest WMAX values found in Fig. 10, despite the latter's enhanced CAPE values. In fact, according to parcel theory, the storms in E2000-V14 have the potential to achieve updraft strengths of  $63 \text{ m s}^{-1}$ , as compared to only  $40 \text{ m s}^{-1}$  in E0800-V12. Another way of looking at this is to realize that in Fig. 10 the

peak convective overturning efficiency values (McCaul and Weisman 1996) only range from 0.27 to 0.56 and never approach the 0.75 value seen in the  $Z_b = Z_v = 2.5$  km simulation in E0800-V12C (Fig. 5).

Figures 11 and 12 contain time series plots from E2000-V14 of selected peak storm parameters, as in Figs. 6 and 7. As in the E0800-V12 cases, the evolution of VMID tends to follow that of WMAX. In the E2000-V14 cases, however, growth of VSFC to its peak value is sometimes quite sudden. These changes in VSFC are apparently related to transient, local fluctuations in the shape and orientation of the surface outflow boundary, and may be very sensitive to model physical parameters that affect the behavior of the downdrafts and surface

$$\text{CAPE}=2000 \text{ J/kg}, V=14 \text{ m/s}$$

(a) ENVIRONMENTAL PARAMETERS (CURVED HODOGRAPHS)		(b) SIMULATED STORM PARAMETERS (CURVED HODOGRAPHS)	
$Z_b=7.1\text{km}$	$Z_b=4.1\text{km}$	$Z_b=7.1\text{km}$	$Z_b=4.1\text{km}$
LI : -5.5 TMAX: 6.0 BRN : 21.6 BSHR: 13.6 HEL : 173 MOT : -4.6,5.0 INFL: 12.1	LI : -6.4 TMAX: 6.6 BRN : 21.6 BSHR: 13.6 HEL : 177 MOT : -4.8,4.4 INFL: 11.6	$Z_v=4.1$ km	TYPE: S-CL WMAX: 26 VORT: 340,194 TOP : 12.8 TMIN: -5.3 ZWMX: 3.8 CORR: 0.65,0.91
			TYPE: S-CL WMAX: 35 VORT: 399,435 TOP : 9.9 TMIN: -7.2 ZWMX: 4.1 CORR: 0.63,0.87
LI : -5.5 TMAX: 6.0 BRN : 44.2 BSHR: 9.5 HEL : 56 MOT : -9.1,4.9 INFL: 8.2	LI : -6.4 TMAX: 6.6 BRN : 44.2 BSHR: 9.5 HEL : 120 MOT : -3.6,6.0 INFL: 12.9	$Z_v=7.0$ km	TYPE: S-CL WMAX: 17 VORT: 312,321 TOP : 13.4 TMIN: -5.5 ZWMX: 3.5 CORR: 0.56,0.91
			TYPE: S-HY WMAX: 27 VORT: 269,235 TOP : 9.9 TMIN: -7.3 ZWMX: 4.2 CORR: 0.52,0.74
(c) ENVIRONMENTAL PARAMETERS (STRAIGHT HODOGRAPHS)		(d) SIMULATED STORM PARAMETERS (STRAIGHT HODOGRAPHS)	
$Z_b=7.1\text{km}$	$Z_b=4.1\text{km}$	$Z_b=7.1\text{km}$	$Z_b=4.1\text{km}$
LI : -5.5 TMAX: 6.0 BRN : 16.5 BSHR: 15.6 HEL : 98 MOT : 4.6,10.0 INFL: 13.9	LI : -6.4 TMAX: 6.6 BRN : 16.5 BSHR: 15.6 HEL : 138 MOT : 6.4,8.5 INFL: 13.3	$Z_v=4.1$ km	TYPE: S-CL WMAX: 24 VORT: 425,247 TOP : 12.2 TMIN: -5.8 ZWMX: 4.3 CORR: 0.46,0.75
			TYPE: S-HP WMAX: 33 VORT: 363,372 TOP : 11.6 TMIN: -7.3 ZWMX: 4.5 CORR: 0.43,0.82
LI : -5.5 TMAX: 6.0 BRN : 39.1 BSHR: 10.1 HEL : 43 MOT : 3.2,9.9 INFL: 12.2	LI : -6.4 TMAX: 6.6 BRN : 39.1 BSHR: 10.1 HEL : 36 MOT : 2.7,7.5 INFL: 9.7	$Z_v=7.0$ km	TYPE: S-CL WMAX: 23 VORT: 304,372 TOP : 13.4 TMIN: -5.6 ZWMX: 4.3 CORR: 0.46,0.76
			TYPE: M WMAX: 25 VORT: 232,253 TOP : 9.9 TMIN: -7.5 ZWMX: 4.3 CORR: 0.40,0.83

FIG. 10. Environmental and storm parameters for the E2000-V14 simulations, as in Fig. 5.

outflow (Wicker and Wilhelmson 1995; Straka and Rasmussen 1998).

In all the large low-level lapse rate cases ( $Z_b = 4.1$  km) from both E2000-V14C and E2000-V14S, but especially those with weak low-level shear ( $Z_v = 7.1$  km), the peak updrafts (WMAX) reach a strong early maximum, then weaken, then redevelop into an often less intense, more episodic regime, suggesting a multicel-

lular character to the convection. All these storms are classed either as HP supercells or multicell squall line storms; the storms having smaller low-level lapse rates are all CL supercell in character. In the multicell case ( $Z_b = 4.1$  km,  $Z_v = 7.1$  km in E2000-V14S), individual cells are too transient to be followed through the entire second hour of the simulations. Peak storm intensity parameters (Fig. 10) for this simulation are therefore

CAPE=2000,  $V=14$ , CURVED, LCL=0.5km  
 TIME SERIES: WMAX, VMID, VSFC, -TMIN

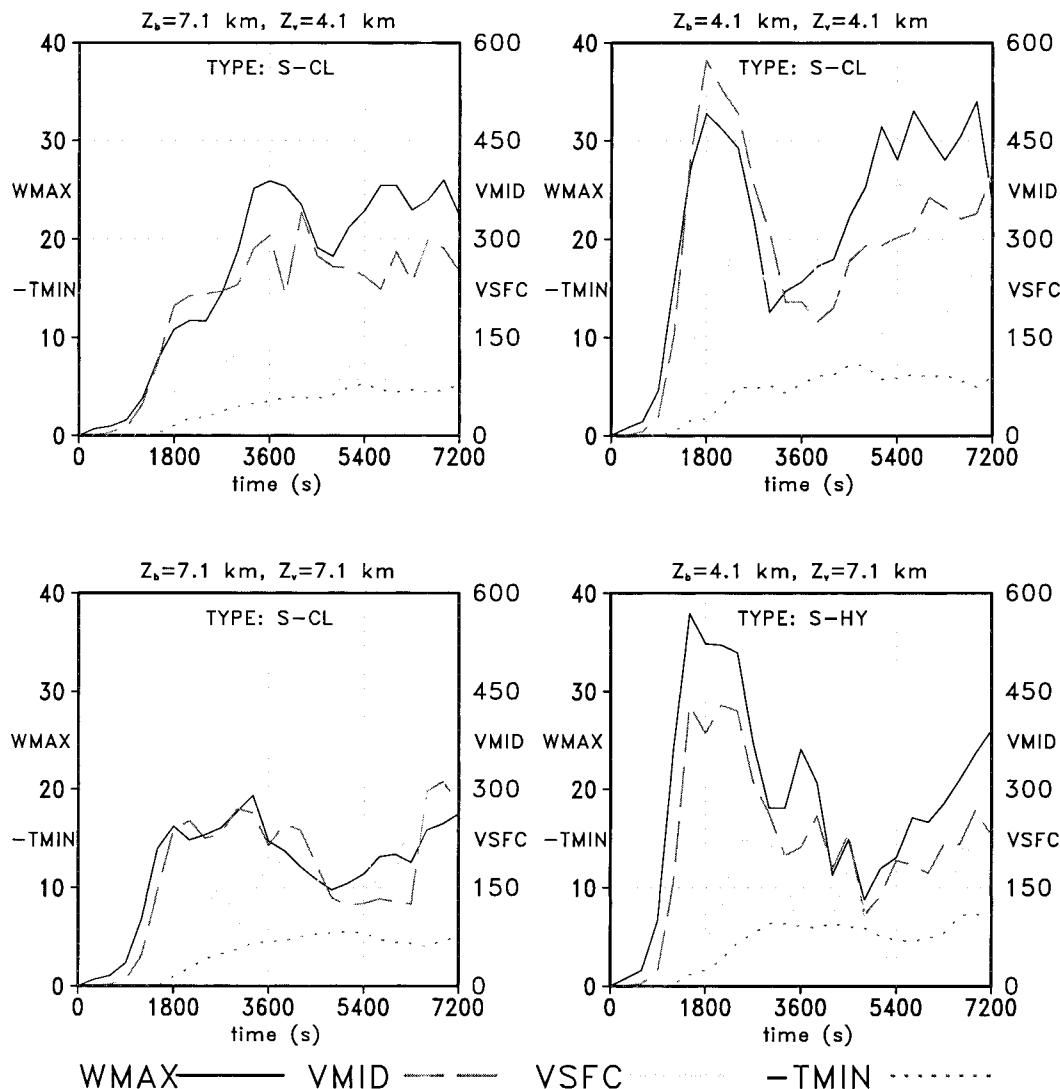


FIG. 11. Evolution of selected storm parameters WMAX, VMID, VSFC, and -TMIN vs time (s) for the E2000-V14C simulations, as in Fig. 6.

obtained from examination of the most dominant cell in the succession of individual multicell members of the most active portion of the line. Likewise, the time series data presented for this simulation (see Fig. 12d) represent the evolution not of one dominant cell, but of the sequence of strong cells mentioned above.

#### 4. Discussion

Although this study does not constitute a complete exploration of the buoyancy-shear profile shape parameter space, a few tentative general conclusions regarding the overall pattern of results may be drawn. First, for a

given choice of bulk CAPE and hodograph trace, there may be considerable sensitivity of storm intensity and morphology parameters to the shapes of the buoyancy and shear profiles, either alone or in combination. In particular, the results from our small CAPE E0800-V12 simulation matrices clearly indicate the existence of a mode of intense but shallow supercellular convection that can occur when both  $Z_b$  and  $Z_v$  are small, that is, when both the buoyancy and ambient vertical shear are concentrated in the lower troposphere. This result confirms and generalizes the speculations of McCaul (1991, 1993) and McCaul and Weisman (1996), which were derived from study of the types of convective storms



CAPE=2000,  $V=14$ , STRAIGHT, LCL=0.5km

TIME SERIES: WMAX, VMID, VSFC, -TMIN

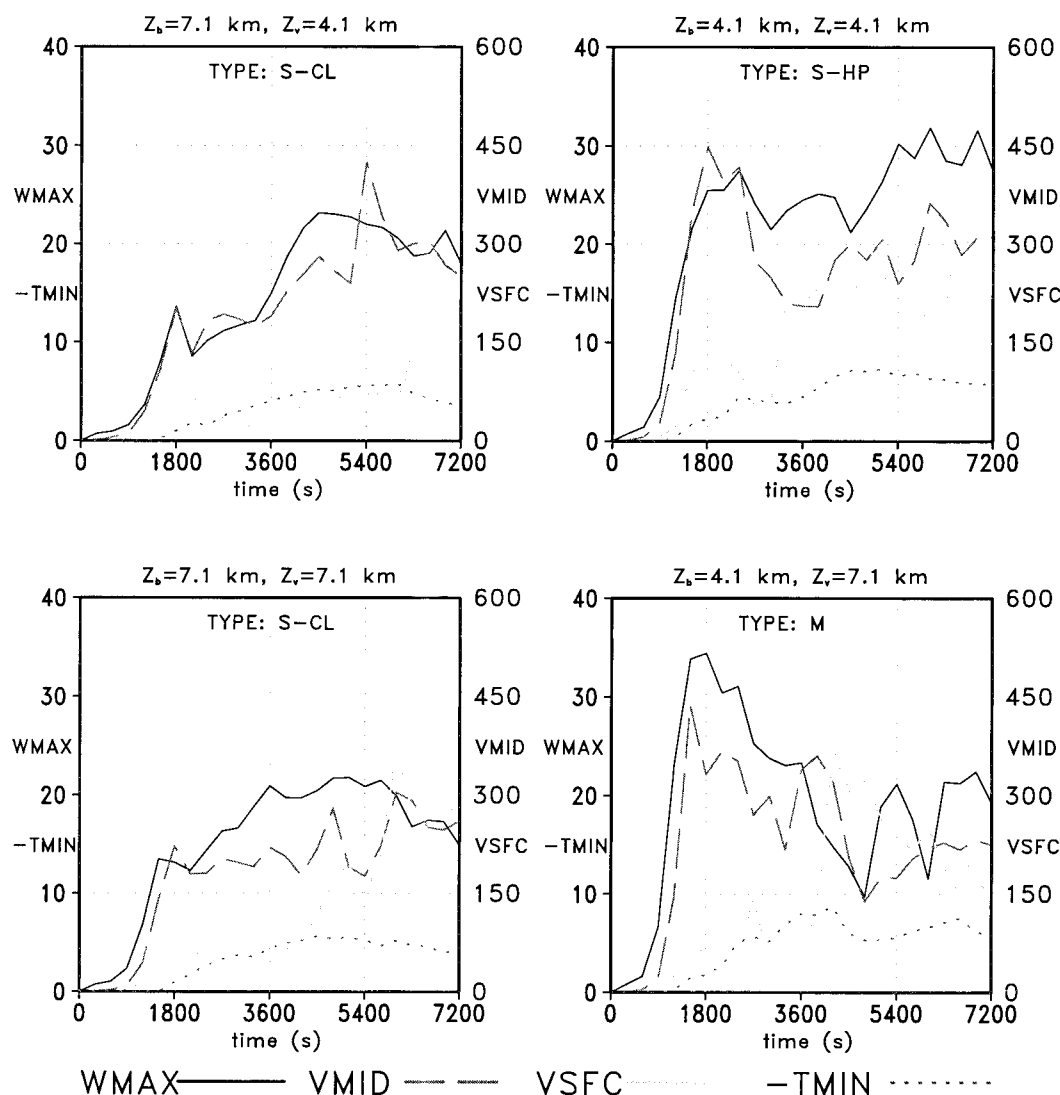


FIG. 12. As in Fig. 11, but for the E2000-V14S simulations.

produced in weak buoyancy environments such as those in landfalling tropical cyclones. In fact, we suspect that the severe weather-producing environments within landfalling tropical cyclones, and also possibly other shallow supercell cases (e.g., McCaul 1987; Davies 1990, 1993; McCaul 1993; Kennedy et al. 1993; Monteverdi and Quadros 1994; McCaul and Weisman 1996), often tend to approximate those found in the small  $Z_b$ , small  $Z_v$  portions of our E0800-V12 simulation matrices.

Gross storm morphological impacts associated with variations in buoyancy and shear profile shapes can be detected through inspection of the field maps in Figs. 3, 4, 8, and 9. The sizes and orientations of the precip-

itation shields relative to the location of the main updraft often show striking differences. Most notable is the tendency for the precipitation shields to intrude into otherwise undisturbed low-level inflow air when low-level shears are strong, and to lie more backward-directed, into the rain-cooled outflow air, when low-level shears are weak. These morphological changes are apparently the result of variations in updraft tilt associated with variations in surface cold pool strength and across-shear propagation rate.

Second, the effect of the buoyancy profile shape on convection is quite strong for small bulk CAPE, where the buoyancy profile is susceptible to specification in a wide variety of ways, but gradually weakens as CAPE

assumes larger and larger values. However, the precise nature of the effect and its synergism with shear appears to depend on the quantitative relationship between the bulk CAPE and bulk shear, as described below. Ultimately, the buoyancy stratification effect must become unimportant in environments featuring extremely large values of CAPE. In the theoretical limiting case of such environments, the buoyancy profile approaches that associated with the virtual temperature difference between a parcel's moist adiabat and its purely dry adiabatic environment, and thus it is not susceptible to any shape variation.

Third, the impact of the variations in the shapes of the buoyancy and shear profiles is not the same for all storm intensity parameters. Changes to the profile shapes that lead to increases in one storm intensity parameter may not lead to increases in another intensity parameter.

Fourth, our results suggest that, for a given bulk CAPE, increasing the ambient lapse rate at low levels has much the same effect on convection as increasing the bulk CAPE, all other things being held constant. This was particularly evident from inspection of the trends in storm intensity in E0800-V12 as  $Z_b$  decreases, versus the trends seen in comparing the results of E0800-V12 against those of E2000-V14. Similarly, increasing the low-level shear within a given hodograph trace, all other things held constant, appears to have much the same effect as increasing the radius of the hodograph trace, a measure of the bulk shear. This is evident from inspection of trends in storm intensity parameters in E2000-V14 as  $Z_v$  decreases. Furthermore, it seems likely that, for any given bulk CAPE and buoyancy and shear profile parameter choice, there is a hodograph trace for which some or all measures of convective storm intensity are maximized, at least for temporally persistent convection. Likewise, for any given hodograph trace and choices of  $Z_b$  and  $Z_v$ , there is a bulk CAPE that tends to maximize the intensity of persistent storms. Environments that do not match these optimum criteria can be said to be either "CAPE starved" (bulk CAPE must be increased, all other things held constant, to realize maximum storm intensity), or "shear-starved" (hodograph trace radius must be increased, all other things held constant, to realize maximum storm intensity). Generally, one also expects that bulk CAPE-starved storms will become more intense if the low-level lapse rates in their environments are increased. Likewise, bulk shear-starved storms should become more intense, at least in their persistent phase, if their low-level shear is augmented. Quantitatively, the enhancements in storm intensity resulting from decreases in  $Z_b$  or  $Z_v$ , with CAPE and hodograph trace held constant, can be substantial, especially when CAPE is small and there is significant CAPE or shear starvation, respectively.

Within the framework of the present environments, we suspect that our E0800-V12 simulations are some-

what CAPE starved. We base this conclusion primarily on the observation that, for those buoyancy and wind-scale altitudes held in common, namely, 4.1 and 5.5 km, storms were seen to increase in intensity when CAPE was increased from 800 to 2000 J kg<sup>-1</sup>, hodograph trace being held constant. This conclusion is also supported by the fact that, within E0800-V12, storm intensity, especially WMAX, exhibits larger increases for a given amount of decrease of the buoyancy scale altitude  $Z_b$  than for a similar decrease in the wind scale altitude  $Z_v$ . In fact, for the small low-level lapse rate cases in E0800-V12, addition of low-level shear essentially prevents the development of persistent convection.

In conjunction with this, we suspect that our E2000-V14 simulations, having 2.5 times as much CAPE, are slightly shear starved. This is hinted at by the occurrence of overt multicell storm behavior within E2000-V14 and by E2000-V12 simulations (not shown), which reveal that the E2000-V14 storms were invigorated by increases in bulk shear. It is easy to imagine from these results that an optimal CAPE and shear profile exists for a given CAPE or shear magnitude, with excessive bulk shear ultimately tending to destroy storms, and excessive CAPE tending to produce increasingly transient and less efficient multicell convective overturning. Weisman and Klemp (1982, 1984) similarly discussed the concept of an optimum balance, although their simulation framework was somewhat different from that employed here. This concept of balance was the motivation they used for proposing the bulk Richardson number, essentially a ratio between CAPE and vertical shear, to characterize supercell potential. It should be noted that it is also possible that the overturning efficiency and thus the degree of CAPE or shear starvation may depend on other parameters of the storm environment, and perhaps also on the details of how various physical processes are treated by cloud models.

In most of our simulations, enhanced peak storm mid-level vorticity VMID tends to be associated with enhanced peak updraft speeds WMAX. This is not surprising, in that WMAX is closely related to the net  $\zeta$  production by updraft stretching of the initially horizontal vorticity that is tilted onto the vertical by the updraft. Both WMAX and VMID are decreasing functions of the buoyancy and wind-scale altitudes  $Z_b$  and  $Z_v$ . In terms of prestorm parameters, some combination of TMAX and BSHR appears to offer the best hope for predictive capability for VMID. Other investigators (Rasmussen and Wilhelmson 1983; Rasmussen and Blanchard 1998) have proposed a "vorticity generation parameter," proportional to the product of (CAPE)<sup>1/2</sup> and a measure of bulk shear, as a tool for forecasting the probability that storms will be supercells. This approach, based loosely on the rate of vorticity production by tilting, may work well in typical midlatitude severe weather environments, where there is often considerable consistency in the shape of the parcel buoyancy profile.

In our present results, however, where large variations

in VMID are apparent in some simulations having the same CAPE, a more elaborate explanation, evidently involving TMAX, is required. In addition, some parameter of the vertical shear, such as BSHR or HEL, is clearly important. BSHR only varies between the rows of simulation matrices, not within those rows, and thus cannot be used to predict the effects of buoyancy profile variations on storm rotation. In general, however, matrix rows having large BSHR tend to have larger mean VMID values. On the other hand, HEL tends to follow variations in VMID most of the time, even within the rows of the simulation matrices, where the wind profile and BSHR are constant. In these simulations, therefore, HEL can only effectively predict the magnitude of mid-level vorticity and does not seem to distinguish the important transitions between supercell and multicell morphology. Its utility as a predictive tool is also limited by the fact that it requires foreknowledge of storm cell motion before it can be evaluated accurately. It is also interesting to note that well-developed supercell storms are sometimes simulated here in environments having surprisingly small values of HEL.

The surface rotation VSFC, on the other hand, tends to exhibit complex behavior. In general, it appears to show some correlation with surface temperature deficit -TMIN, which is strongly tied to TMAX, a parameter that is in turn regulated by the choice of  $Z_b$ . Indeed, if we examine all the simulation pairs having identical  $Z_b$  in Figs. 3 and 8, and exclude from consideration the storms that are multicell or hybrid, it is seen that VSFC always increases when  $Z_b$  decreases. This tends to support the notion that, at least in horizontally homogeneous starting environments, the most important factor associated with near-surface mesocyclogenesis in supercells is baroclinic generation of horizontal streamwise vorticity in the inflow regions of storm updrafts (Rotunno and Klemp 1985), which is then available to be converted into vertical vorticity by tilting. Baroclinic zones associated with surface cold pools also tend to be coincident with areas of strong horizontal shear and vertical vorticity produced through the collision of diverging downdraft air at the surface with inflow air, and this can also contribute to near-surface and surface mesocyclogenesis, and perhaps tornadogenesis.

The variation of peak surface vorticity VSFC with low-level lapse rates and vertical shear, especially in the straight hodograph regimes that display evidence of CAPE starvation, suggests that in some cases strong low-level shear may in fact be a deterrent to tornado formation. While it appears that variations in the strength of the subcloud baroclinity and the orientation of low-level horizontal ambient vorticity vectors (Wicker 1996) can explain at least some of these variations in surface mesocyclone strength, complete understanding of this and of the differences between the straight and curved hodograph cases requires additional detailed investigation.

In practice, most observed severe storm environmen-

tal profiles are noisy enough that it is easier to characterize their CAPE than their altitudes of maximum buoyancy and wind. It would be convenient if integral quantities such as CAPE or HEL could be used to forecast the potential for VSFC growth. Indeed, comparison of our small CAPE and large CAPE results shows that generally larger values of VSFC occur for the latter. However, TMAX (and -TMIN) are also larger for the large CAPE cases. It is through consideration of intra-matrix results, where CAPE and hodograph trace are fixed, that we are led to conclude that TMAX (and -TMIN) is of comparable importance to VSFC as CAPE. This conclusion is tempered, however, by the realization that VSFC may not be a perfect surrogate for the likelihood of tornadogenesis, and that our simulations are based on highly simplified microphysics, which may limit the realism of the downdrafts and outflows, and hence VSFC, in our results. Clearly, further study of these relationships is required before simulation results such as those presented here can be applied with confidence to the problem of tornado forecasting.

The present results also reveal that storm motion shows sensitivity to the buoyancy profile shape, especially when CAPE is small or the hodograph curved. This is described in Fig. 13, where representative storm cell motions from the second hour of the simulations are plotted on hodographs. These cell motions were determined by averaging the motions of the dominant cell over the longest available period of time during hour 2 for which the motions were quasi-steady. Inspection of Fig. 13 reveals that, at small CAPE, storm motions MOT tend to deviate most from the hodograph when the low-level lapse rates are largest. This deviant motion is maximized when low-level shears are also strong. The transient storms seen when low-level shears are strong but low-level lapse rates are small display only small deviant motions, which suggests their inability to establish an effective link to the dynamical potential of their kinematic environments.

At large CAPE, the amount of off-hodograph deviant motion again appears to be largely governed by the low-level lapse rates, with the exception of the multicell case in the straight hodograph regime. For this particular storm, the outflow boundary propagation is in some sense too large for the storm's deviant motion-producing dynamical capability, and each successive cell in the multicell progression falls behind the outflow, slows down, and then dissipates. For the small lapse-rate supercell cases, low-level shear magnitude again appears to produce enhanced deviant motion.

The influence of the strength of the vertical shear on storm motion, mediated by pressure gradient accelerations on the flanks of rotating updrafts (Rotunno and Klemp 1985), is a familiar result, but the influence of low-level lapse rate has never been explored quantitatively. In general, we find that increases in the low-level lapse rate tend to produce both stronger updraft rotation and colder surface outflows, and more rapid storm cell

## STORM MOTIONS ON HODOGRAPHS

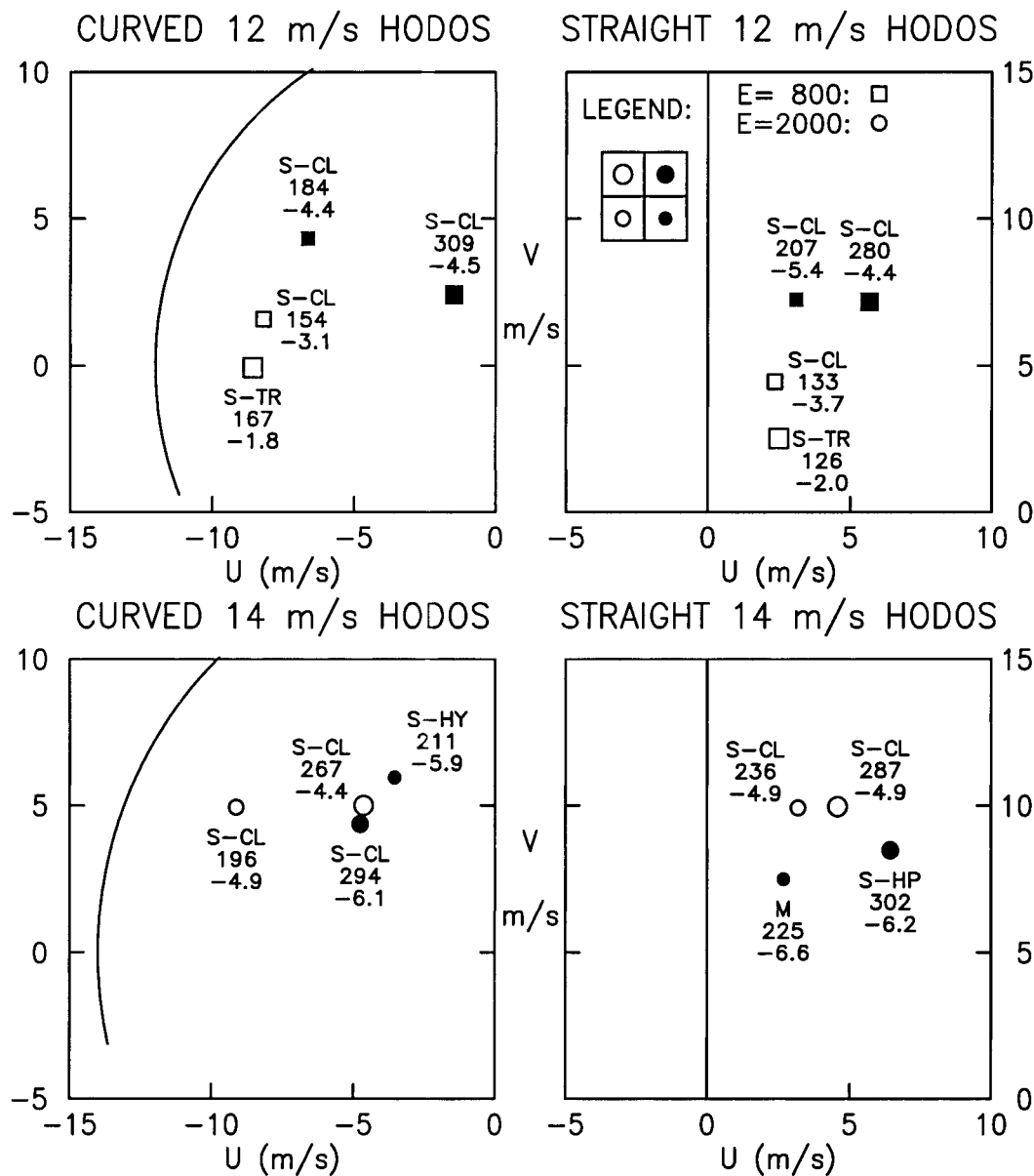


FIG. 13. Representative storm cell motions during second hour of simulations, as depicted on subregions of environmental hodographs. Squares and circles represent the storm motions, with enhanced symbol size implying enhanced environmental vertical shear, darkened symbols implying enhanced low-level buoyancy and lapse rates, and symbol shape corresponding to the amount of CAPE. These graphical conventions are indicated in the matrixlike legend in the upper right panel. Upper panels describe results for hodographs having a radius parameter of  $12 \text{ m s}^{-1}$  and contain data from only  $\text{CAPE} = 800 \text{ J kg}^{-1}$  simulations. Lower panels describe storm motions for hodographs with radius parameter of  $14 \text{ m s}^{-1}$ , where only  $\text{CAPE} = 2000 \text{ J kg}^{-1}$  simulations were performed. Also shown adjacent to each storm motion symbol are storm TYPE, and the mean values of midlevel vorticity VMID and near-surface perturbation potential temperature TMIN for the periods during which storm motions were evaluated.

propagation relative to the low-level ambient wind, at least for the cases where supercells are found. Study of the mean VMID and TMIN data provided in Fig. 13 suggests that cell deviant motion is indeed more closely related to VMID than to TMIN. However, for large

CAPE cases with low-level shears too weak relative to the low-level lapse rates, deviant motions associated with cell rotation cannot match outflow boundary motion, and true supercells become unsustainable. These findings may have implications for commonly used fore-



casting rules of thumb purporting to predict cell motion solely based on consideration of the hodograph. It may also help explain the difficulty in forecasting the propagation of HP supercell storms based on hodograph structure alone (Bunkers et al. 1998). Further research in this area is needed to clarify the limiting conditions required to support storm propagation dynamics consistent with surface cold pool propagation dynamics.

In all our simulations, the vertical shears were chosen to be of sufficient strength to make updraft rotation likely. Thus, it is not surprising to find evidence of supercell structure in many of our results. Nevertheless, there exists a wide variation in size and intensity of these supercells, and in the number and arrangement of the storm cells in each simulation domain. Except for the finding that supercell-like storms with strong surface mesocyclones can exist even in weak buoyancy environments, our results are generally consistent with previous storm morphology research (Weisman and Klemp 1982, 1984), with 18 of 22 BRN-based morphology predictions correct if the  $40 \leq \text{BRN} \leq 50$  cases are omitted. The present results, while generally confirmative of prior findings, also suggest a need to generalize the BRN theory further by accounting for the influence of both buoyancy and wind profile shape on peak storm updraft and midlevel mesocyclone vorticity.

While the simulated storms described here exhibit significant differences in morphology and intensity, the results suffer from limitations that make direct application to storm forecasting difficult. For instance, because horizontal homogeneity was assumed for starting conditions, the results are most applicable to isolated convective cells. Furthermore, the model employed in this study contains no ice physics. However, we reiterate that preliminary inspection of a subset of simulation results obtained from a model with full ice microphysics (C. Cohen 1999, personal communication) has confirmed the existence of the principal sensitivities described here.

Finally, despite the apparent robustness of our results, we emphasize that it is premature to attempt to apply these findings to generalized storm environments. All the simulations reported herein featured a rather low level of free convection (LFC) of just under 0.5 km altitude AGL. Sensitivity tests conducted by us indicate a strong dependence of storm intensity and morphology to changes in either the LFC or the lifted condensation level, with the strongest updrafts being associated with environments where the LFC is located at higher altitudes than those used here. Exploration of this particular sensitivity is relegated to a future report.

## 5. Summary and outlook

These simulation results show that variations in the stratification of buoyancy, with or without concomitant variations in the shear stratification, can have a major impact on the intensity of simulated convective storms,

when CAPE, hodograph trace, level of free convection, and the profile of relative humidity are all held constant. The effect is particularly strong in small CAPE environments, partly because there is much more flexibility in specifying the shape of the buoyancy profile in such environments. However, the effect also occurs in stronger CAPE environments, at least for the wind profiles considered in this study.

In our results, we find that all the basic storm intensity parameters—updraft intensity, peak midlevel and surface vorticity, and surface cold outflow—exhibit sensitivity to variations in the shapes of both the buoyancy and wind profiles. These sensitivities themselves appear to vary with some measure of the balance between environmental bulk values of CAPE and shear: When an environment is in some sense CAPE starved, then compression of the buoyancy into the lower troposphere can at least partially compensate, and likewise, when an environment is shear starved, compression of the shear into the lower levels can at least partially compensate.

The present results suggest a need for much further exploration of these profile shape effects. Future work should focus on the following areas: 1) Predictability of the surface outflow and vorticity fields as functions of model resolution, initialization, and microphysics; 2) assessment of the storms' momentum, energy and vorticity budgets (Lilly and Jewett 1990), and entrainment rates, and their dependence on the environmental profile shapes; 3) extension of these results to a wider range of CAPE and wind profiles, with consideration given to possibly important variations in upper-level shear (Rasmussen and Straka 1998); 4) extension of these results to environments having layers of drier air aloft (see, e.g., Gilmore and Wicker 1998); 5) extension of these results to environments having varying levels of free convection, with consideration of how entrainment effects are impacted; and 6) generation of theoretical concepts capable of encompassing all the results in a minimum number of simple physical principles. Finally, there are the important observational questions of validating the model results and of learning how often the real atmosphere visits each part of profile-shape parameter space.

Our results may also have implications for areas of research other than severe storm dynamics. One such possible area is that of cumulus parameterization in large-scale models. Our results may also help explain the observed weakness of convection in the oceanic Tropics, where buoyancy often exists in small amplitude through a deep layer, but what little shear there is exists mainly at low levels (Lucas et al. 1994). In the meantime, other investigators using numerical simulations to study convective storm dynamics as a function of varying environmental parameters should take steps to ensure that their results are not inadvertently contaminated by stratification effects such as those described here.

*Acknowledgments.* The present work was begun in

1989 by EWM under National Science Foundation Grant ATM890001N for access to Cray supercomputers at the National Center for Supercomputing Applications at the University of Illinois, Urbana–Champaign. Preliminary results documenting the validity of the simulation approach and showing how the buoyancy and shear profile shapes affected storms at small CAPE were obtained in early 1990, while the first author was supported by a postdoctoral fellowship in the Advanced Study Program at the National Center for Atmospheric Research. The final full simulations were performed on NCAR Cray supercomputers. EWM wishes to acknowledge the support and interest of Doug Lilly, Bob Wilhelmson, Joe Klemp, Rich Rotunno, John Firor, Howie Bluestein, Bob Davies-Jones, Stan Trier, Bill Skamarock, and many other colleagues during the course of completion of this research. Special thanks are due to Doug Lilly, Stan Trier, Bill Skamarock, and anonymous reviewers, whose careful proofreading prompted us to find and clear up some errors and other inadequacies in earlier versions of this work.

## APPENDIX

### Construction of Environmental Profiles

We prescribe the parcel buoyancy  $b$ , relative to assumed pseudoadiabatic ascent, in terms of an analytical function of altitude  $z' = z - z_L$ , where  $z$  is standard altitude AGL and  $z_L$  is a prespecified altitude of the lifting condensation level (LCL) for parcels initially located at the second model level ( $k = 2$ ) above the surface. Our choice of functional form for  $b(z')$  is given by

$$b(z') = E \frac{m^2}{H^2} z' \exp\left(-\frac{m}{H} z'\right), \quad (\text{A1})$$

where  $E$  is a specified CAPE,  $H$  is a vertical scale, and  $m$  is a profile compression parameter. For these simulations, we have  $E = 800$  or  $2000 \text{ J kg}^{-1}$ ;  $H = 14.5 \text{ km}$ ; and pressure, temperature, and dewpoint at  $k = 2$  of  $965 \text{ hPa}$ ,  $23.5^\circ\text{C}$ , and  $23.0^\circ\text{C}$ , respectively, such that  $z_L = 0.454 \text{ km}$ . We also specify  $m = 2.9, 4.0$ , or  $7.0$  for the  $E = 800$  cases, and  $m = 2.2, 2.9$ , or  $4.0$  for the  $E = 2000$  cases. Within these two trios of choices of  $b$  profile shape parameter  $m$ , two of the values,  $m = 2.9$  and  $m = 4.0$ , are identical, but the other values differ. It was not possible to make all three values of  $m$  be identical for both CAPE regimes without compromising our ability to explore the limiting buoyancy lapse rate case  $m = 7.0$  for the small CAPE regime, or violating the physical realizability of the simulations. For example, the use of  $m = 7.0$  in the large CAPE environment would have implied a superadiabatic lapse rate at low levels, which was unacceptable from both a physical and a numerical simulation standpoint. In addition, the use of  $m = 2.2$  in the small CAPE environment would have led to parcel buoyancies too small to support per-

sistent convection in our simulations. Incomplete overlap of the values of  $m$  is therefore unavoidable when our approach is used to specify buoyancy profiles for thorough exploration of environments having very different CAPEs.

From (A1) it is easy to show that the altitude above the LCL of maximum  $b$  is  $H/m$ , so that our choices for  $m$  and  $z_L$  imply buoyancy maxima at the altitudes  $Z_b = 7.05, 5.45, 4.08$ , and  $2.53 \text{ km AGL}$ , respectively. Our inability to use large values of  $m$  in the large CAPE environments corresponds to an inability to construct profiles having very small  $Z_b$  there. It should be noted that, because we include no inversions in our starting environments, the LCL is always equal to the LFC in this study.

Note that in (A1) the vertical integral of  $b$  from the LCL to a very great height is  $E$  and is independent of the parameter  $m$ , thus ensuring conservation of CAPE for a given  $E$  across all possible choices of  $m$ . In our simulations, however, we specify a tropopause at an altitude of  $14.0 \text{ km}$ , overlaid by an isothermal stratosphere. This truncates the profiles of  $b$  somewhat, leading to values of CAPE that vary with  $m$ . To circumvent this problem and force each profile to have the same CAPE, we compute the CAPE  $E_i$  of each truncated profile and evaluate the ratio  $E/E_i$ , and multiply each buoyancy profile by this ratio. At the end of this procedure, the maximum buoyancy in each profile is  $b_{\max} = (E/E_i)(m/H)E \exp(-1)$ , which when converted to perturbation potential temperature  $\theta'$  yields values, as computed on our model mesh, of  $2.3^\circ, 2.5^\circ$ , and  $3.8^\circ\text{C}$ , for the three  $m$  choices used in the small CAPE simulations, or  $6.0^\circ, 6.0^\circ$ , and  $6.6^\circ\text{C}$  for those used in the large CAPE simulations. Thus, our procedure yields profiles that exhibit variations in the maximum buoyancy as well as the altitude at which it occurs. The shapes of all our profiles are illustrated in Fig. 1, and selected standard environmental parameters for the key simulations within each matrix are furnished along with other simulation data in Figs. 10 and 5, which summarize each set of simulation results. It should be noted that many other analytical functions could have been used in place of (A1), although we found our choice in (A1) to be advantageous because of its simplicity and because it contains only one inflection point, which causes all the buoyancy and wind profiles to have their largest rates of change with height occur at cloud base.

For moisture above the LCL, we prescribe a profile of constant 90% relative humidity in each simulation so as to minimize the complications associated with the many possible variations of environmental moisture that may occur for any given temperature profile, a topic that is not the subject of this study. Mixing ratios  $q_v$  are then assigned by applying the Clausius–Clapeyron equation to the already obtained temperature and relative humidity profiles. Temperatures and mixing ratios in the subcloud layer are obtained by constructing  $\theta$  and  $q_v$  profiles there that feature both (a) constant equivalent

potential temperature and (b) Richardson numbers larger than the model's critical value for the most strongly sheared wind case. The latter constraint ensures that our simulations never trigger spontaneous turbulent instabilities in the ambient environment. The subcloud profiles of temperature and moisture are identical for all simulations.

It should be noted that our specification of thermodynamic conditions thus dictates that CAPE computed assuming ascent of a surface parcel is equal to that computed from parcels ascending from levels  $k = 1$  or  $k = 2$ . In addition, if we assume a mixed layer equal in depth to the altitude  $z_L$ , nearly 500 m, the CAPE computed from conditions in the mixed layer would also be identical to the first two types of CAPE. All CAPE computations described here include the virtual temperature effects of water vapor, but exclude those associated with condensate loading, and thus correspond to CAPE values used in operational weather forecasting environments.

Our curved hodographs are based on a  $v$  wind component that has the same general height-dependent structure as does  $b$ , but with the constraint  $v_{\max} = V =$  constant for each choice of wind compression parameter  $n$  in place of the constant vertical integral constraint used for  $b$ . Once the  $v$  profile is specified, the  $u$  profile for the circularly curved hodographs follows from the assumption that the total wind speed is constant and equal to  $V$  at each level. Thus our curved hodograph wind components ( $u_c, v_c$ ) are obtained from

$$v_c(z') = c(n)V \frac{n^2}{H^2} z' \exp\left(-\frac{n}{H} z'\right) \quad \text{and} \quad (\text{A2})$$

$$u_c(z') = \text{sgn}(z' - Z_v) \{V^2 - [v_c(z')]^2\}^{1/2}, \quad (\text{A3})$$

where we have chosen  $V = 12$  or  $14 \text{ m s}^{-1}$ ,  $H = 14.5 \text{ km}$ , with  $n$  having the same values as  $m$  given earlier. The factor  $c(n) = n^{-1} \exp(1)$  is required to ensure each  $v$  profile reaches a maximum value of  $V$  for any choice of  $n$ , and the  $\text{sgn}$  factor determines the sign that is applied to the square root. Comparison of (A2) with (A1) shows that the  $v_c$  component reaches its maximum at altitudes  $Z_v$  that assume the same values as those cited earlier for  $Z_b$ . Thus, more shear is concentrated at low levels as  $n$  increases. Our choices of  $V$  yield shear profiles of moderate intensity, with bulk Richardson numbers spanning both the multicell and supercell regimes predicted by Weisman and Klemp (1982, 1984).

For the straight hodograph cases, we set  $u_s = 0$  and assign  $v_s$  values based on the chord lengths of level-to-level segments of the curved hodographs defined by (A2) and (A3). This strategy guarantees that the total discretized shears in the curved and straight hodograph cases are similar for similar values of  $n$ . An approximate formula for  $v_s$  may be written under the assumption that the chord lengths of the discretized curved hodographs become infinitesimally small, in which case we find

$$v_s(z') = V \arcsin\left(\frac{v_c}{V}\right). \quad (\text{A4})$$

Note that for the straight hodographs, although the wind profiles change shape with  $n$ , the corresponding altitudes  $Z_v$  associated with (A2) no longer represent levels of maximum  $v$ . For the straight hodographs, the  $v$  component always increases with height.

## REFERENCES

- Brooks, H. E., C. A. Doswell III, and R. B. Wilhelmson, 1994: The role of midtropospheric winds in the evolution and maintenance of low-level mesocyclones. *Mon. Wea. Rev.*, **122**, 126–136.
- Bunkers, M. J., B. A. Klimowski, J. W. Zeitler, R. L. Thompson, and M. L. Weisman, 1998: Predicting supercell motion using hodograph techniques. Preprints, *19th Conf. on Severe Local Storms*, Minneapolis, MN, Amer. Meteor. Soc., 611–614.
- Davies, J., 1990: Midget supercell spawns tornadoes. *Weatherwise*, **43**, 260–261.
- , 1993: Small tornadic supercells in the Central Plains. Preprints, *17th Conf. on Severe Local Storms*, St. Louis, MO, Amer. Meteor. Soc., 305–309.
- Davies-Jones, R., D. Burgess, and M. Foster, 1990: Test of helicity as a tornado forecast parameter. Preprints, *16th Conf. on Severe Local Storms*, Kananaskis Park, AB, Canada, Amer. Meteor. Soc., 588–592.
- Doswell, C. A., III, and D. W. Burgess, 1993: Tornadoes and tornadic storms: A review of conceptual models. *The Tornado: Its Structure, Dynamics, Prediction, and Hazards*, C. R. Church, Ed., Amer. Geophys. Union, 119–142.
- Droegemeier, K. K., S. M. Lazarus, and R. Davies-Jones, 1993: The influence of helicity on numerically simulated convective storms. *Mon. Wea. Rev.*, **121**, 2005–2029.
- Gilmore, M. S., and L. J. Wicker, 1998: The influence of midtropospheric dryness on supercell morphology and evolution. *Mon. Wea. Rev.*, **126**, 943–958.
- Jewett, B. F., R. B. Wilhelmson, J. M. Straka, and L. J. Wicker, 1990: Impact of ice parameterization on the low-level structure of modeled supercell thunderstorms. Preprints, *16th Conf. on Severe Local Storms*, Kananaskis Park, AB, Canada, Amer. Meteor. Soc., 275–280.
- Kennedy, P. C., N. E. Westcott, and R. W. Scott, 1993: Single-Doppler radar observations of a mini-supercell tornadic thunderstorm. *Mon. Wea. Rev.*, **121**, 1860–1870.
- Klemp, J. B., and R. B. Wilhelmson, 1978: The simulation of three-dimensional convective storm dynamics. *J. Atmos. Sci.*, **35**, 1070–1096.
- Knupp, K., J. Stalker, and E. W. McCaul Jr., 1998: An observational and numerical study of a mini-supercell storm. *Atmos. Res.*, **49**, 35–63.
- Lilly, D. K., 1986: The structure, energetics and propagation of rotating convective storms. Part II: Helicity and storm stabilization. *J. Atmos. Sci.*, **43**, 126–140.
- , and B. F. Jewett, 1990: Momentum and kinetic energy budgets of simulated supercell thunderstorms. *J. Atmos. Sci.*, **47**, 707–726.
- Lucas, C., E. J. Zipser, and M. A. LeMone, 1994: Vertical velocity in oceanic convection off tropical Australia. *J. Atmos. Sci.*, **51**, 3183–3193.
- McCaul, E. W., Jr., 1991: Buoyancy and shear characteristics of hurricane tornado environments. *Mon. Wea. Rev.*, **119**, 1954–1978.
- , 1993: Observations and simulations of hurricane-spawned tornadic storms. *The Tornado: Its Structure, Dynamics, Prediction, and Hazards*, C. R. Church, Ed., Amer. Geophys. Union, 119–142.
- , and M. L. Weisman, 1996: Simulations of shallow supercell

- storms in landfalling hurricane environments. *Mon. Wea. Rev.*, **124**, 408–429.
- Moller, A. R., C. A. Doswell III, M. P. Foster, and G. R. Woodall, 1994: The operational recognition of supercell thunderstorm environments and storm structures. *Wea. Forecasting*, **9**, 327–347.
- Monteverdi, J. P., and J. Quadros, 1994: Convective and rotational parameters associated with three tornado episodes in northern and central California. *Wea. Forecasting*, **9**, 285–300.
- Rasmussen, E. N., and R. B. Wilhelmson, 1983: Relationships between storm characteristics and 1200 GMT hodographs. Preprints, *13th Conf. on Severe Local Storms*, Tulsa, OK, Amer. Meteor. Soc., J5–J8.
- , and D. O. Blanchard, 1998: A baseline climatology of sounding-derived supercell and tornado forecasting parameters. *Wea. Forecasting*, **13**, 1148–1164.
- , and J. M. Straka, 1998: Variations in supercell structure. Part I: Observations of the role of upper-level storm-relative flow. *Mon. Wea. Rev.*, **126**, 2406–2421.
- Richardson, Y. P., K. K. Droegemeier, and R. Davies-Jones, 1998: A study of the influence of horizontally varying vertical shear and CAPE on numerically simulated convective storms. Preprints, *19th Conf. on Severe Local Storms*, Minneapolis, MN, Amer. Meteor. Soc., 249–252.
- Rotunno, R., and J. B. Klemp, 1985: On the rotation and propagation of simulated supercell thunderstorms. *J. Atmos. Sci.*, **42**, 271–292.
- Schlesinger, R. E., 1978: A three-dimensional numerical model of an isolated thunderstorm: Part I. Comparative experiments for variable ambient wind shear. *J. Atmos. Sci.*, **35**, 690–713.
- Straka, J. M., and E. N. Rasmussen, 1998: Thirty years of cloud modeling: Does the emperor wear clothes? Preprints, *19th Conf. on Severe Local Storms*, Minneapolis, MN, Amer. Meteor. Soc., 342–347.
- , Y. Liu, and L. J. Wicker, 1993: The influence of ice-phase microphysics on convective storm structure and evolution. Preprints, *17th Conf. on Severe Local Storms*, St. Louis, MO, Amer. Meteor. Soc., 178–183.
- Weisman, M. L., and J. B. Klemp, 1982: The dependence of numerically simulated convective storms on vertical wind shear and buoyancy. *Mon. Wea. Rev.*, **110**, 504–520.
- , and ———, 1984: The structure and classification of numerically simulated convective storms in directionally varying shears. *Mon. Wea. Rev.*, **112**, 2479–2498.
- Wicker, L. J., 1996: The role of near-surface wind shear on low-level mesocyclone generation and tornadoes. Preprints, *18th Conf. on Severe Local Storms*, San Francisco, CA, Amer. Meteor. Soc., 115–119.
- , and R. B. Wilhelmson, 1995: Simulation and analysis of tornado development and decay within a three-dimensional supercell thunderstorm. *J. Atmos. Sci.*, **52**, 2675–2703.
- Wilhelmson, R. B., and C. S. Chen, 1982: A simulation of the development of successive cells along a cold outflow boundary. *J. Atmos. Sci.*, **39**, 1466–1483.